

Analytical Reformulation of Angles-only Measurements with Application to Cislunar Object Tracking

Nicholas H. Craig ^{*} and Kenshiro Oguri [†]
Purdue University, West Lafayette, Indiana, 47906

This paper proposes a robust alternative approach to fusing information from angles-only measurements into sequential filters. It has become common practice to work directly with the azimuth and elevation of an object in the local visual field to construct measurement residuals for use within batch or sequential filters. While easy to obtain, these values can prove troublesome particularly in scenarios where measurements are scarce and intermittently available. This is due primarily to the linear approximation of the measurement function breaking down when the residual is too large. This study introduces a filter working measurement and associated error covariance, constructed from the measured azimuth and elevation, that eliminates the non-linearity in the measurement function while preserving the angular uncertainty. Additionally, it will be shown that this approach can be generalized to work with received range-only measurements and a fusion of independent range and angular measurements. A final comparison between the traditional non-linear measurement equations and the proposed variable-range pointing vector is performed for cislunar uncooperative object tracking scenarios with intermittent measurements due to various observation exclusion zones.

Nomenclature

\mathbf{X}	=	Non-dimensional spacecraft state in synodic frame
\mathbf{r}	=	Non-dimensional position in synodic frame
U^*	=	CR3BP pseudo-potential function
μ	=	Non-dimensional system mass constant
$\hat{\mathbf{X}}, \hat{\mathbf{Y}}, \hat{\mathbf{Z}}$	=	Frame basis vectors
\mathbf{Z}	=	Noisy measurement vector
θ	=	Azimuth

An earlier version of this paper was presented as paper 25-393 at the 2025 AAS/AIAA Space Flight Mechanics Meeting, Kaua'i, HI, January 19-23 2025

^{*}M.S. Student, School of Aeronautics and Astronautics, Purdue University, 701 W. Stadium Ave. West Lafayette, IN 47906

[†]Assistant Professor, School of Aeronautics and Astronautics, Purdue University, 701 W. Stadium Ave. West Lafayette, IN 47906, and Member AIAA

ϕ	=	Elevation
\mathbf{v}	=	Additive measurement noise
σ	=	Standard deviation
ψ	=	Boresight and conjunction angles
δ	=	Angular atmospheric refraction term
ΔM	=	Object apparent magnitude
I	=	Object irradiance as observed by sensor
F	=	Radiant flux density
λ	=	Wavelength
QE	=	Sensor quantum efficiency
Ψ	=	Object phase function
γ	=	Sun-object-observer phase angle
ν	=	Body eclipse shadow function
\mathbf{Z}^*	=	Pointing vector pseudo-measurement
$\hat{\lambda}$	=	Measurement noise rotation vector
α	=	Measurement noise rotation angle
P	=	Covariance matrix
S	=	Covariance Cholesky
\mathbf{f}	=	State dynamics
B	=	Process noise mapping matrix
\mathbf{h}	=	State to measurement mapping function
\mathbf{g}	=	Received measurement to pseudo-measurement mapping function
F	=	State dynamics jacobian
H	=	Measurement mapping jacobian
\mathbf{y}	=	Information state
Λ	=	Information matrix

Subscripts and Superscripts

H	=	Hill Frame
S	=	Sensor Frame
rel	=	Relative position to observer
bsg	=	Sensor boresight axis
$\odot, \oplus, \mathbb{C}$	=	Sun, Earth, Moon

FoR = Field of Regard
* = Pointing vector variant

I. Introduction

VISUAL based observations have long been used to track and predict the motion of the planets. Kepler himself used tables of angular measurements of Mars' position in the night to come up with his elliptical orbit model [1]. Today we use cameras and telescopes to track thousands of small bodies in orbit about Earth and even more in our solar system[2]. Because of this widespread adoption, many different algorithms have been developed for both initial and precise orbit determination[3].

Although optically based measurements such as azimuth and elevation are easy to obtain and geometrically intuitive, their non-linear mathematical representation has been a common source of issue within initial orbit determination (IOD) and precise orbit determination (POD) algorithms. In the past POD algorithms have commonly implemented via some sort of Gaussian, central moment based, filter such as the Extended Kalman Filter (EKF) and Unscented Kalman Filter (UKF), along with their information and square root variants[3]. However, as the system dynamics and measurement models become increasingly non-linear these traditionally linear algorithms begin to falter. In an attempt to circumvent these issues there has been a recent push for more non-Gaussian probability density function (pdf) characterizations. One such approach is known as a Gaussian mixture (GM) model. Here, rather than predict the first and second order moments (mean and covariance) of the pdf, GM models attempt to fully characterize the higher order moments via a summation of many small Gaussian distributions [4, 5]. Implementation of azimuth/elevation measurements within these algorithms for spacecraft navigation has become widely adopted in industry, and for certain dynamical systems such as the circular restricted three body problem (CR3BP), it has been shown to yield an observable system[6]. That being said, angles-only navigation is not without its own challenges. Filters implementing highly non-linear measurements can often struggle in their initial convergence and in situations where there are significant periods of occlusion. This is in part due to the high non-linearity of the function that maps the state of interest to the measured azimuth and elevation. In scenarios like this, and when implementing a Gaussian filter (EKF), it has become common practice in industry to implement what is known as underweighting or damping of a filter[7, 8]. In essence, an underweighted filter reduces the magnitude of the state and error covariance update when the predicted measurement error covariance is comparatively large to the known error covariance. While underweighting is a powerful tool, it does require an additional tuning parameter that can be cumbersome to determine.

Returning to the problem at hand, in the case where range measurements are available in addition to angles, one approach to eliminate the non-linearity of the measurement mapping function is to transform the values into a Cartesian relative position vector and use the measurement Jacobian to transform the error covariance from range and

azimuth/elevation to position [9, 10]. If range is unavailable, a similar approach can be taken except the magnitude of the Cartesian vector is normalized[11]. However, in this case the unit Cartesian vector remains a non-linear measurement of the state and, as will be discussed later, the error covariance matrix becomes rank deficient. Furthermore, all of the above approaches assume that the measurement noise is zero-mean, Gaussian and additive to azimuth, elevation, and range if available. While extensive implementation has shown that this measurement error model does work, it is not a truly accurate representation of the angular uncertainty associated with line of sight measurements[12].

This paper proposes a new pseudo-measurement that addresses these problems while better characterizing the measurement error in the covariance matrix. This pseudo-measurement, called the *variable-range pointing vector*, is computed from the measured azimuth and elevation as well as the predicted range of the object to generate an expected position measurement. Similarly, the pointing vector (PV) error covariance is produced such that the angular uncertainty inherent to line of sight measurements is preserved. The approach of including existing information within a reformulation of measurements or covariances is not new. Crassidis[13] takes a similar approach but for the dual attitude position determination problem. Similarly, the measurement error characterization derived in this paper is shown to be equivalent to those proposed by Shuster[12] and Crassidis. As the PV takes on the form of the object's relative position, the state to PV measurement mapping function is linear. Finally, because the PV measurement and error covariance are transformations of the actual measurements, this approach can be used to augment substantially more advanced filters such as those developed in Ref. 4, 5.

Through the mathematical derivation of the pointing vector it becomes clear that this problem formulation has certain similarities to the early algorithms developed for attitude determination. Here, it is common practice for star trackers, sun sensors, magnetometers, etc. to measure a unit vector in a body fixed frame. The goal being to find the rotation matrix that best maps the known vectors in an inertial frame to the measured vectors in the body frame. One of the first and most widely adopted methods to solve this was the TRIAD algorithm[14]. This approach allows for a deterministic evaluation of the rotation matrix from two measured unit vectors. In the derivation of the associated covariance matrix, Shuster[12] makes the assumption of axially symmetric noise to these vectors and formulates the angular uncertainty to the first order in Cartesian space. The TRIAD algorithm was widely adopted in the early years of satellite operations due to its fast and deterministic nature. Unfortunately, it was designed to work with only two measurements and must discard some of the information contained within one. The problem of attitude determination quickly shifted to an optimization problem of finding the matrix that best fits any number of measured vectors. Thus was born Wahba's problem[15]. Here, attitude determination is stipulated as an optimization problem of finding the rotation matrix that minimizes a least squares cost function of N observed vectors. Although a solution was originally proposed, it was Davenport's[16, 17] *q-method* reformulation of the problem that gained significant traction within the community. Rather than solving the optimization problem of Wahba, Davenport recasts it as finding the maximum eigenvalue of an augmented matrix of vector observations with the associated eigenvector taking the form of the attitude quaternion.

With increasing interest in cis-lunar operations, precise knowledge of all bodies therein is paramount. Inspired by Ref. 18, 19, we consider a Moon-based cislunar object tracking scenario. Here an observer located at a fixed point on the Moon attempts to track a spacecraft in an unknown trajectory using only the initial state estimate along with sequential measurements of the azimuth and elevation of its position. To increase model fidelity, a number of visibility checks are performed to include the sensors field of regard, object occlusion with the Earth and Sun, and the objects relative brightness. To examine the converged filter characteristics such as root mean squared error (RMSE), only periodic orbits in cis-lunar space will be considered for the spacecraft's true trajectory. Thus a repeatable framework to compare the two measurement methodologies is established.

II. Background

A. Reference Frames

There are two frames used in this paper. First of which is the rotating Hill frame for use within the dynamics model. Denoted by a left superscript H , the $\hat{\mathbf{X}}$ -axis points from the Earth to the Moon, the $\hat{\mathbf{Z}}$ -axis points along the angular momentum vector of the Moon's orbit about the Earth, and the $\hat{\mathbf{Y}}$ -axis such that a complete right hand basis set is formed. This Hill frame is centered at the Earth-Moon barycenter and is seen in Figure 1. The second frame is the sensor-frame, denoted S . This frame is formed via a 3-2 rotation sequence from the Hill frame where the first rotation is through the measured azimuth, and the second rotation is through the negative of the measured elevation. This results in the $\hat{\mathbf{X}}_S$ -axis pointing towards the spacecraft of interest, and the $\hat{\mathbf{Y}}_S/\hat{\mathbf{Z}}_S$ -axes being tangential to the local visual sphere Figure 2.

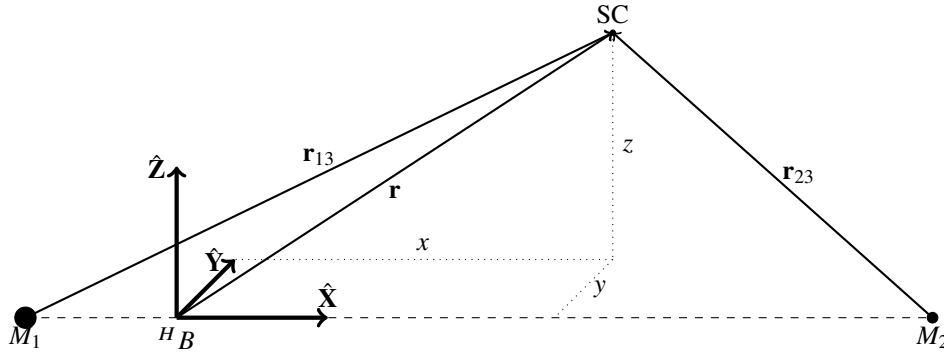


Fig. 1 Circular Restricted 3 Body Problem

B. Circular Restricted Three Body Problem

While the focus of this paper is not of dynamical systems, a brief overview of the dynamics is provided below. As spacecraft depart the Earth environment, the assumption of Keplerian dynamics breaks down rather quickly[20]. To include the gravitational field of the Moon, the circular restricted three body problem (CR3BP) is used as the dynamical

model. The spacecraft's (SC) non-dimensional state is its position and velocity within the Hill frame.

$${}^H\mathbf{X} = \begin{bmatrix} x & y & z & \dot{x} & \dot{y} & \dot{z} \end{bmatrix}^\top \quad (1)$$

In this frame the governing equations of motion (with respect to the non-dimensionalized time) are:

$$\ddot{x} = 2\dot{y} + \frac{\partial U^*}{\partial x} \quad (2a)$$

$$\ddot{y} = -2\dot{x} + \frac{\partial U^*}{\partial y} \quad (2b)$$

$$\ddot{z} = \frac{\partial U^*}{\partial z} \quad (2c)$$

$$U^* = \frac{1-\mu}{r_{13}} + \frac{\mu}{r_{23}} + \frac{x^2 + y^2}{2} \quad (2d)$$

where μ is known as the non-dimensional mass of the Moon, and r_{13} and r_{23} are the distances from the SC to the Earth and Moon respectively.

$$\mu = \frac{m_2}{m^*} \quad (3a)$$

$$m^* = m_1 + m_2 \quad (3b)$$

$$l^* = D_1 + D_2 \quad (3c)$$

$$t^* = \sqrt{\frac{l^{*3}}{Gm^*}} \quad (3d)$$

$$\mathbf{r}_{13} = (x + \mu)\hat{\mathbf{X}} + y\hat{\mathbf{Y}} + z\hat{\mathbf{Z}}, \quad r_{13} = \|\mathbf{r}_{13}\| \quad (3e)$$

$$\mathbf{r}_{23} = (x - 1 + \mu)\hat{\mathbf{X}} + y\hat{\mathbf{Y}} + z\hat{\mathbf{Z}}, \quad r_{23} = \|\mathbf{r}_{23}\| \quad (3f)$$

Three additional characteristic quantities are defined, m^* , l^* and t^* that relate the non-dimensional mass, length, and time to their dimensional counterparts.

C. Measurement Models

As was discussed within the introduction, the focus of this paper is to propose an alternate way of fusing angular and range measurements within traditional sequential filtering algorithms. With that, a brief overview of the traditional measurement models will be discussed below for use within future comparisons.

1. Angle-Only Measurements

As with many orbit determination schemes, it is often the case that only visual based observations are available. For the purposes of this study we assume two angles are available as measurements when the SC is visible. These are the

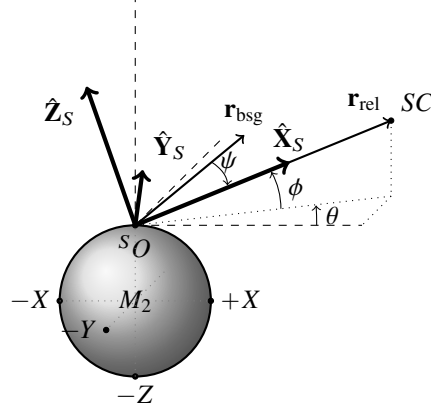


Fig. 2 Moon Based Observer

azimuth and elevation from an observer on the Moon's surface. With the location of the observer given as \mathbf{r}_O in the Hill frame, the measured azimuth θ and elevation ϕ are then calculated as:

$$\mathbf{Z} = \begin{bmatrix} \theta \\ \phi \end{bmatrix} = \begin{bmatrix} \tan^{-1} \left(\frac{y-y_O}{x-x_O} \right) \\ \sin^{-1} \left(\frac{z-z_O}{\|\mathbf{r}-\mathbf{r}_O\|} \right) \end{bmatrix} + \mathbf{v} \quad (4a)$$

$$\mathbf{v} = \begin{bmatrix} \mathcal{N}(0, \sigma_\theta) \\ \mathcal{N}(0, \sigma_\phi) \end{bmatrix} \quad (4b)$$

where \mathbf{v} is additive noise commonly characterized as zero mean and Gaussian for its simplicity. This assumption however, is quite inaccurate. Physically, this can be observed in Figure 3 where two different reference line of sight (LoS) vectors are considered: a. the measurement is near-equatorial ($\phi \approx 0^\circ$) and b. the measurement is near a pole ($\phi \approx \pm 90^\circ$).

The discrepancy observed above is a nice visual representation of both the nonlinearity in the state-to-measurement mapping functions, as well as the geometrical impact of the Gaussian errors in azimuth and elevation. Ideally we would like our observation errors to reflect those in Figure 4(a) but regardless of the direction of the LoS vector. First noted by Schuster[12], a more accurate assumption in the error of visual-based observations is one that assumes that all error follows a bi-variate Gaussian distributed in the plane normal to the LoS vector. This originally came from a first-order approximation of unit-vectors for use within star trackers and attitude determination. A more thorough derivation for this characterization of the angular error will be proposed later for the pointing vector. While these quantities are rather intuitive to work with, their mathematical representation with respect to a Cartesian state is regrettably, quite nonlinear. This will become particularly evident in later sections.

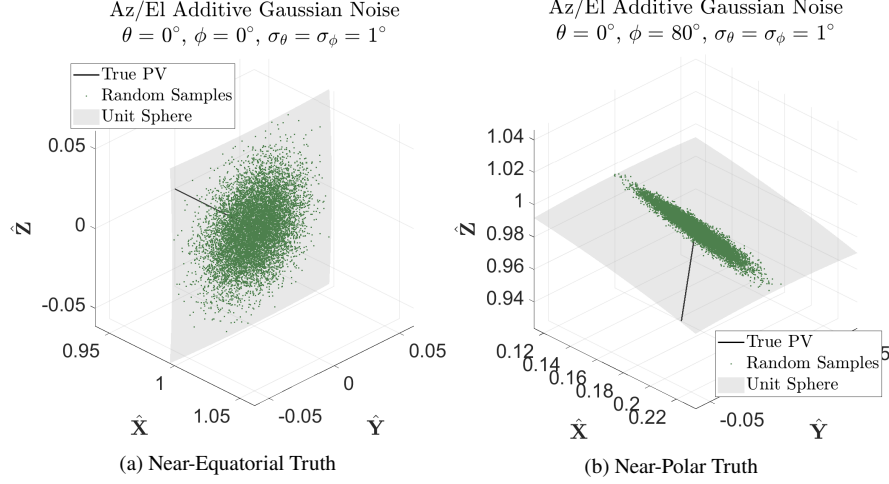


Fig. 3 Gaussian Azimuth and Elevation Error Distribution

2. Range-Only Measurements

Another, albeit less common, measurement for use within space-based autonomous navigation and tracking is range. Range-only IOD and POD algorithms are well studied at this point and still see regular use today[21, 22] especially when radio-based measurements are used. The standard range measurement non-linear mapping function is given below.

$$\mathbf{Z} = r_{\text{rel}} + \mathbf{v} \quad (5a)$$

$$r_{\text{rel}} = \sqrt{\mathbf{r}_{\text{rel}}^T \mathbf{r}_{\text{rel}}} = \sqrt{(x - x_O)^2 + (y - y_O)^2 + (z - z_O)^2} \quad (5b)$$

$$\mathbf{v} = \mathcal{N}(0, \sigma_{\text{rng}}) \quad (5c)$$

In comparison to the angular measurements, the range formulation does look more well behaved. However, because the range formulation contains information in only one dimension, we may expect a range-only POD filter to provided a less robust navigation solution when compared to a similarly tuned angles-only filter.

3. Range and Angle Measurement Fusion

The last measurement model that we will include in this analysis is a combination of both range and angular measurements. Here, it is assumed that the measurements received are independently gathered range, azimuth, and elevation. The problem of range and angle measurement fusion is well studied at this point. Two of the most common approaches in current literature are either to perform the filter update twice for each set of measurements or to combine them into a position measurement and convert the error covariances over via a form of a first order Taylor-series expansion [10].

While the focus of this paper is on an alternate angles-only navigation and tracking technique, we also show the

capability of the pointing vector with range-only measurements and a fusion of both range and angles.

D. Object Visibility

Common with any visually-based observations such as from a camera, telescope or radar, obtaining a measurement is first limited to whether or not the SC can be seen. Here we will use four visibility checks: sensor field of regard, SC occlusion with the Earth and Sun, and the relative brightness of the SC. If any of these cases are met we assume that no measurement is available.

1. Sensor Field of Regard

The angle between the SC position vector relative to the observer \mathbf{r}_{rel} and the fixed bore sight vector of the observer \mathbf{r}_{bsg} is determined via:

$$\mathbf{r}_{\text{rel}} = \mathbf{r} - \mathbf{r}_O \quad (6a)$$

$$\psi_{\text{FoR}} = \text{atan2}(\|\mathbf{r}_{\text{rel}} \times \mathbf{r}_{\text{bsg}}\|, \mathbf{r}_{\text{rel}}^\top \mathbf{r}_{\text{bsg}}) \quad (6b)$$

When $\psi_{\text{FoR}} > \psi_{\text{FoR,lim}}$, the spacecraft is not visible and thus no measurement can be collected.

2. Body Conjunction

Similar to the FoR check, body conjunction occurs when the spacecraft passes either in front or behind one of the primary bodies. Mathematically, this is equivalent to the SC-observer-body phase angle dropping beneath some threshold. The phase angle is a function of the object's position and the primary body's position, both relative to the observer.

$$\psi_{\oplus/\odot} = \text{atan2}(\|\mathbf{r}_{\text{rel}} \times \mathbf{r}_{\text{rel},\oplus/\odot}\|, \mathbf{r}_{\text{rel}}^\top \mathbf{r}_{\text{rel},\oplus/\odot}) \quad (7a)$$

$$\psi_{\oplus/\odot,\text{lim}} = \text{atan}\left(\frac{R_{\oplus/\odot}}{r_{\text{rel},\oplus/\odot}}\right) + \delta_{\oplus/\odot} \quad (7b)$$

Here δ represents an extra angular region about the body, due to atmospheric refraction, where the object cannot be distinguished from the background light. It is assumed that $\delta_{\oplus} = 0.35$ for any Earth conjunctions and $\delta_{\odot} = 0.525$ for any Sun conjunctions. When $\psi_{\oplus/\odot} < \psi_{\oplus/\odot,\text{lim}}$ the spacecraft is not visible and no measurement is available.

3. Relative Brightness

The final visibility test checks if the SC is sufficiently bright to be able to distinguish it amongst the background radiation. To aid with this, there are a couple of key assumptions made: the SC[23], Earth[24] and Moon are diffusely reflecting spheres, the Sun's spectral irradiance is modeled via Planck's law of black body radiation, and the limiting

magnitude of the sensor is approximated using the human pupil as a baseline[25].

As is common in astronomy, the brightness check will be done using the spacecraft's apparent magnitude rather than its irradiance directly. The apparent magnitude with respect to some background radiation source is given below.

$$\Delta M = -2.5 \log_{10} \left(\frac{I_{SC}}{I_0} \right) \quad (8)$$

Where I_{SC} is the irradiance of the SC as observed by the sensor, and I_0 is the irradiance of Vega ($I_0 = 2.51802 \cdot 10^{-8} \left[\frac{W}{m^2} \right]$)[25]. As mentioned, the limiting magnitude is obtained by comparing the telescope aperture diameter to that of the human pupil (approximately 7 mm).

$$M_{lim} \approx 2 + 5 \log_{10}(D[\text{mm}]) \quad (9)$$

Assuming a telescope diameter of 1.5 meters yields a magnitude limit of ≈ 17 . If $\Delta M > M_{lim}$ then the spacecraft is taken to be too dim and thus not visible.

The SC irradiance is solved for by integrating the radiant flux density incident on the spacecraft as seen by the observer, $F(\lambda) \left[\frac{W}{m^3} \right]$, multiplied by the sensor's quantum efficiency, $QE(\lambda)$, through the full wavelength (λ) radiation band.

$$I_{SC} = \int F(\lambda) \cdot QE(\lambda) d\lambda \quad (10a)$$

$$F(\lambda) = F_{\odot}(\lambda) + F_{\oplus}(\lambda) + F_{\zeta}(\lambda) \quad (10b)$$

An optical sensor's quantum efficiency curve is a measure of how well a particular wavelength of light can be converted from photons to electrons within the photo-diode. It is common practice for the QE of a sensor to be reported for either separate bands (e.g. red, green, blue) or for the full monochromatic spectrum. When multiplied by the radiant flux density of the illuminated object, this can be thought of as the intensity of the object as viewed by the sensor for a specific wavelength. For the purposes of this study we assume the sensor holds the properties outlined in [26].

The radiant flux density $F(\lambda)$ is comprised from 3 different light sources: direct sunlight, Earth-reflected sunlight and Moon-reflected sunlight. As mentioned, it is assumed that the Sun's irradiance takes on the approximate form of a black body radiator. Thus, the direct sunlight, radiant flux density incident on the spacecraft, as seen from the observer, is

$$F_{\odot}(\lambda) = \underbrace{\left(\frac{2hc^2}{\lambda^5} \frac{1}{\exp\left(\frac{hc}{\lambda k T_{\odot}}\right) - 1} \right)}_{a)} \underbrace{\left(\frac{\pi R_{\odot}^2}{r_{\odot 2SC}^2} \right)}_{b)} \underbrace{\left(\frac{\Psi}{r_{rel}^2} \right)}_{c)} \underbrace{(v_{\oplus} \cdot v_{\zeta})}_{d)} \quad (11)$$

where a) is Planck's law for a black body radiator (k is Boltzman's constant, h is Planck's constant, c is the speed of light

in a vacuum, and T_{\odot} is the black body temperature of the sun) and b) accounts for the cross sectional area of the Sun and the space loss between the SC and Sun (R_{\odot} is the Sun's radius, and $r_{\odot 2SC}$ is the distance between the sun and SC). Term c) includes the SC phase-function (Ψ) as well as the space loss to the observer. Throughout this study it is assumed that the spacecraft can be appropriately modeled as a Lambertian diffusely reflecting sphere [23].

$$\Psi(\gamma) = \frac{2}{3} \frac{C_d R_{SC}^2}{\pi} (\sin(\gamma) + (\pi - \gamma) \cos(\gamma)) \quad (12)$$

where C_d is the spacecraft coefficient of diffuse reflectivity and γ is the Sun-SC-Observer phase angle. The final term d) is the shadow function (v_{\oplus}/v_{ζ}) of any Earth and Moon eclipses[27].

$$v_{\oplus/\zeta} = 1 - \frac{A}{\pi a^2} \quad (13a)$$

$$A = a^2 \cos^{-1} \left(\frac{x}{a} \right) + b^2 \cos^{-1} \left(\frac{c-x}{b} \right) - cy \quad (13b)$$

$$a = \sin^{-1} \left(\frac{R_{\odot}}{|\mathbf{r}_{\odot} - \mathbf{r}|} \right) \quad (13c)$$

$$b = \sin^{-1} \left(\frac{R_{\oplus/\zeta}}{s} \right) \quad (13d)$$

$$c = \cos^{-1} \left(\frac{-\mathbf{s}^T (\mathbf{r}_{\odot} - \mathbf{r})}{s |\mathbf{r}_{\odot} - \mathbf{r}|} \right) \quad (13e)$$

$$\mathbf{s} = \mathbf{r} - \mathbf{r}_{\oplus/\zeta} \quad (13f)$$

$$x = \frac{c^2 + a^2 - b^2}{2c} \quad (13g)$$

$$y = \sqrt{a^2 - x^2} \quad (13h)$$

The flux density equations for the Earth and Moon Reflected sunlight are very similar to that of Equation (11) except the b) term is replaced with an adaption from [24]. Here Cunningham[24] approximates the body reflected light via a spherical surface integral across the area of the body that is both illuminated by the sun and visible to the object. The result of this integration is a scalar, existing on the interval $[0, 1]$, that represents the fraction of the sun reflected light incident on the spacecraft. Lastly, when accounting for the Earth and Moon reflected light, the "emitter" depending on the geometry, could be circular but will more often than not take the form of a crescent. Because the shadow function derived in [27] assumes the overlap of two spherical projections, the low likelihood of one body eclipsing the other, and the overall small contribution of body reflected light to the object, we assume $v_{\oplus} = v_{\zeta} = 1$ for Earth and Moon reflected light.

III. Variable Range Pointing Vector

A. Error Modeling

With more interest in passive and uncooperative target tracking, use of cameras and optical sensors for this purpose has surged. While the model of azimuth/elevation additive noise has worked in the past, it does not properly address the noise that many optical based sensors experience. When considering a camera observing the location of a body in its field of view or grouping of pixels on its sensor, the noise associated with the measured azimuth and elevation is more aptly characterized as a cone of angular uncertainty about the line of sight vector[12]. Equivalently, this can be thought of as all the error existing in the plane normal to the LoS vector. This is because when an object is observed on a camera's sensor, there is uncertainty in alignment with the sensor's pixels. If a bi-variate Gaussian distribution is assumed in the plane of the camera's sensor, the error distribution becomes generally elliptic. This leads to the elliptical/circular angular cone of uncertainty. Modeling this angular uncertainty for azimuth and elevation analytically is troublesome as it is not immediately evident how one would vary these elements to achieve such a distribution. Consider instead a pseudo-measurement, called the pointing vector (PV), defined as a function of the measured azimuth and elevation. This is also scaled by, for the moment, some arbitrary length r .

$$\bar{\mathbf{Z}}^* = r \begin{bmatrix} c_\phi c_\theta \\ c_\phi s_\theta \\ s_\phi \end{bmatrix} \quad (14)$$

where the bar represents the mean or expected value and $c_\theta = \cos \theta$, $s_\theta = \sin \theta$. Under the assumption that the noise is zero mean, this pseudo-measurement on average becomes a vector pointing from the sensor to the spacecraft.

With this as the new working measurement within the filter, angular noise can be re-characterized as a rotation of $\bar{\mathbf{Z}}^*$ about a random normal vector $\hat{\lambda}$ by some random angle α . To define $\hat{\lambda}$, the sensor-frame needs to be established via a Euler angle 3-2 rotation sequence through angles θ and $-\phi$. This rotation matrix was strategically chosen such that the $\hat{\mathbf{X}}_S$ -axis of the sensor-frame is aligned with the pointing vector. Consequently, this necessitates that the plane formed by $\hat{\mathbf{Y}}_S/\hat{\mathbf{Z}}_S$ is orthogonal to the pointing vector, $\bar{\mathbf{Z}}^*$. The direction cosine matrix (DCM) associated with this

rotation sequence is:

$$\begin{aligned}
[HS] &= R_2(-\phi)R_3(\theta) = \begin{bmatrix} c_\phi & 0 & s_\phi \\ 0 & 1 & 0 \\ -s_\phi & 0 & c_\phi \end{bmatrix} \begin{bmatrix} c_\theta & s_\theta & 0 \\ -s_\theta & c_\theta & 0 \\ 0 & 0 & 1 \end{bmatrix} \\
&= \begin{bmatrix} c_\phi c_\theta & c_\phi s_\theta & s_\phi \\ -s_\theta & c_\theta & 0 \\ -s_\phi c_\theta & -s_\phi s_\theta & c_\phi \end{bmatrix} = \begin{bmatrix} \hat{\mathbf{X}}_S^\top \\ \hat{\mathbf{Y}}_S^\top \\ \hat{\mathbf{Z}}_S^\top \end{bmatrix}
\end{aligned} \tag{15}$$

Using this sensor-frame, $\hat{\lambda}$ is written as a random unit vector lying in the $\bar{\mathbf{Z}}^*$ -normal plane given by the sensor $\hat{\mathbf{Y}}_S/\hat{\mathbf{Z}}_S$ -axes. Expressed in the hill-frame, these axes are given as a function of θ and ϕ and are the second and third row of the DCM $[HS]$. Such a vector $\hat{\lambda}$ is then fully characterized by random angle ω off of the $\hat{\mathbf{Y}}_S$ -axis.

$$\hat{\lambda} = c_\omega \hat{\mathbf{Y}}_S + s_\omega \hat{\mathbf{Z}}_S = c_\omega \begin{bmatrix} -s_\theta \\ c_\theta \\ 0 \end{bmatrix} + s_\omega \begin{bmatrix} -s_\phi c_\theta \\ -s_\phi s_\theta \\ c_\phi \end{bmatrix} = \begin{bmatrix} \lambda_1 \\ \lambda_2 \\ \lambda_3 \end{bmatrix} \tag{16}$$

Recall that the angular noise is more appropriately described as a rotation of $\bar{\mathbf{Z}}^*$ about a random normal vector, characterized by the variable ω , by a small random angle α . This transformation is known as Euler's rotation theorem[28]. The corresponding DCM, defined as the measurement noise $[MN]$, is well known and generally given as:

$$[MN] = \begin{bmatrix} \lambda_1^2(1 - c_\alpha) + c_\alpha & \lambda_1\lambda_2(1 - c_\alpha) + \lambda_3s_\alpha & \lambda_1\lambda_3(1 - c_\alpha) - \lambda_2s_\alpha \\ \lambda_2\lambda_1(1 - c_\alpha) - \lambda_3s_\alpha & \lambda_2^2(1 - c_\alpha) + c_\alpha & \lambda_2\lambda_3(1 - c_\alpha) + \lambda_1s_\alpha \\ \lambda_3\lambda_1(1 - c_\alpha) + \lambda_2s_\alpha & \lambda_3\lambda_2(1 - c_\alpha) - \lambda_1s_\alpha & \lambda_3^2(1 - c_\alpha) + c_\alpha \end{bmatrix} \tag{17}$$

For most tracking applications, the relative angular uncertainty is small, that is $\alpha \ll 1^\circ$. Under the small-angle approximation we take $c_\alpha \approx 1$ and $s_\alpha \approx \alpha$. Substituting these approximations into Equation (17) considerably simplifies the DCM to:

$$[MN] \approx \begin{bmatrix} 1 & \alpha\lambda_3 & -\alpha\lambda_2 \\ -\alpha\lambda_3 & 1 & \alpha\lambda_1 \\ \alpha\lambda_2 & -\alpha\lambda_1 & 1 \end{bmatrix} \tag{18}$$

The pointing vector corrupted by angular noise is then given as a multiplication of the true vector $\bar{\mathbf{Z}}^*$ with the

measurement noise $[MN]$.

$$\mathbf{Z}^* = [MN] \bar{\mathbf{Z}}^* \quad (19)$$

In fact, under the small angle approximation, this multiplication equates to a linear addition of noise. By using Equations (16), (18) and (19) the noisy pointing vector measurement is evaluated below.

$$\begin{aligned} \mathbf{Z}^* &= \begin{bmatrix} 1 & \alpha(s_\omega c_\phi) & -\alpha(c_\omega c_\theta - s_\omega s_\phi s_\theta) \\ -\alpha(s_\omega c_\phi) & 1 & \alpha(-c_\omega s_\theta - s_\omega s_\phi c_\theta) \\ \alpha(c_\omega c_\theta - s_\omega s_\phi s_\theta) & -\alpha(-c_\omega s_\theta - s_\omega s_\phi c_\theta) & 1 \end{bmatrix} r \begin{bmatrix} c_\phi c_\theta \\ c_\phi s_\theta \\ s_\phi \end{bmatrix} \\ &= r \begin{bmatrix} c_\phi c_\theta + \alpha(s_\omega c_\phi) c_\phi s_\theta - \alpha(c_\omega c_\theta - s_\omega s_\phi s_\theta) s_\phi \\ -\alpha(s_\omega c_\phi) c_\phi c_\theta + c_\phi s_\theta + \alpha(-c_\omega s_\theta - s_\omega s_\phi c_\theta) s_\phi \\ \alpha(c_\omega c_\theta - s_\omega s_\phi s_\theta) c_\phi c_\theta - \alpha(-c_\omega s_\theta - s_\omega s_\phi c_\theta) c_\phi s_\theta + s_\phi \end{bmatrix} \\ &= r \begin{bmatrix} c_\phi c_\theta \\ c_\phi s_\theta \\ s_\phi \end{bmatrix} + r\alpha c_\omega \begin{bmatrix} -c_\theta s_\phi \\ -s_\theta s_\phi \\ c_\theta^2 c_\phi + s_\theta^2 c_\phi \end{bmatrix} + r\alpha s_\omega \begin{bmatrix} c_\phi^2 s_\theta + s_\phi^2 s_\theta \\ -c_\phi^2 c_\theta - s_\phi^2 c_\theta \\ 0 \end{bmatrix} \\ &= r \begin{bmatrix} c_\phi c_\theta \\ c_\phi s_\theta \\ s_\phi \end{bmatrix} + r\alpha c_\omega \begin{bmatrix} -c_\theta s_\phi \\ -s_\theta s_\phi \\ c_\phi \end{bmatrix} + r\alpha s_\omega \begin{bmatrix} s_\theta \\ -c_\theta \\ 0 \end{bmatrix} \end{aligned}$$

It is clear that when working with the pointing vector formulation, the angular noise takes the form of simple addition of two vectors to the measurement. The only assumption made thus far is that the angular uncertainty is small

$$\mathbf{Z}^* = \bar{\mathbf{Z}}^* + \alpha c_\omega \mathbf{v}_1 + \alpha s_\omega \mathbf{v}_2 \quad (20a)$$

$$\mathbf{v}_1 = r \begin{bmatrix} -c_\theta s_\phi \\ -s_\theta s_\phi \\ c_\phi \end{bmatrix}, \quad \mathbf{v}_2 = r \begin{bmatrix} s_\theta \\ -c_\theta \\ 0 \end{bmatrix} \quad (20b)$$

Up to this point r is an undefined deterministic value, while α and ω are random variables that characterize the angular uncertainty. Noticing that both of these values appear as the polar form of a two-dimensional position, a change of variable is helpful where $\alpha_x = \alpha c_\omega$ and $\alpha_y = \alpha s_\omega$. Each of these scalars represents the angle by which the pointing

vector is rotated in the two sensor-plane directions.

$$\mathbf{Z}^* = \bar{\mathbf{Z}}^* + \alpha_x \mathbf{v}_1 + \alpha_y \mathbf{v}_2 \quad (21)$$

This can be intuited as the uncertainty in the horizontal and vertical directions of the pixels in a camera's sensor. It is assumed that this noise is unbiased and follows a bi-variate Gaussian distribution[12]. These two values are similar to the uncertainty in azimuth/elevation as they are angular in nature, however the strength of this approach is that under this formulation the angular uncertainty takes the form of a circular, or more generally elliptical, cone about the true pointing vector.

$$\alpha_x \sim \mathcal{N}(0, \sigma_x), \quad \alpha_y \sim \mathcal{N}(0, \sigma_y) \quad (22)$$

Here σ_x and σ_y are the standard deviations of the angular uncertainty in the sensor's $\hat{\mathbf{Y}}_S$ and $\hat{\mathbf{Z}}_S$ axes respectively. For example, it is common in industry for commercial off the shelf star-trackers to provide on their spec sheet a value (typically in arc-seconds) for the one standard-deviation pointing accuracy of the sensor. In such a case, this number would be used for both σ_x and σ_y . This implies that a star-tracker reporting the azimuth and elevation (or cartesian unit vector) of a star in its visual field expects there to be an angular uncertainty about the line of sight vector of standard deviation $\sigma_x = \sigma_y$.

Returning to the issue of the Gaussian error assumption in azimuth and elevation presented in Section II.C.1, let us consider the geometric error distribution using the pointing vector model. Provided in Figure 4 are the same two LoS vectors but with the new pointing vector angular noise model.

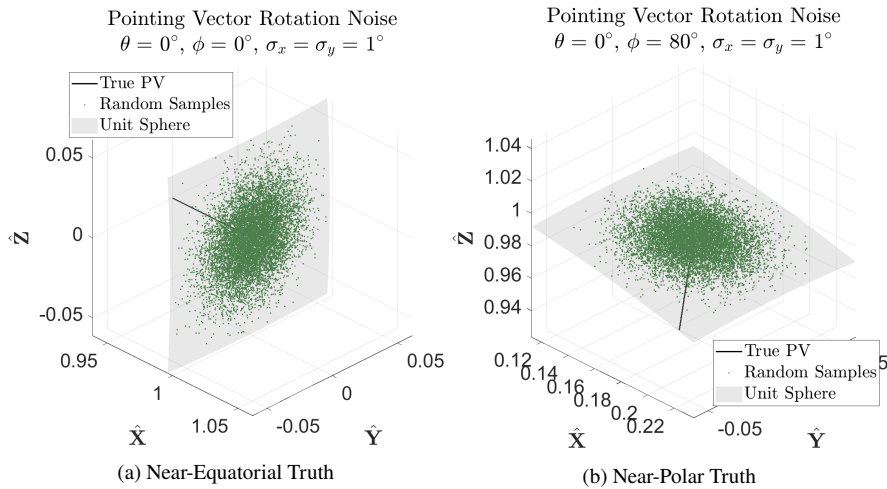


Fig. 4 Gaussian Pointing Vector Error Distribution

As was desired, this measurement and noise model allows for a generally elliptical error distribution in the LoS vector similar to that proposed by Schuster[12].

B. Covariance Analysis

As with any other measurement, implementation within filtering algorithms requires the characterization of the error uncertainty in the form of a covariance matrix. Traditionally it is common to use a constant covariance matrix that is often supplied by the sensor manufacturer. However, in our formulation because the pointing vector is a transform of the received measurements, the covariance matrix must be evaluated for by using the azimuth and elevation measurements $[\theta, \phi]$, the known angular uncertainty of the sensor σ_x and σ_y as well as the currently arbitrary scalar r . Generally, the covariance of a random vector \mathbf{X} is given as:

$$P = \mathbb{E} \{ (\mathbf{X} - \mathbb{E}\{\mathbf{X}\})(\mathbf{X} - \mathbb{E}\{\mathbf{X}\})^\top \} \quad (23)$$

Substituting in \mathbf{Z}^* for \mathbf{X} it is immediately clear that the expectation value of the noisy pointing vector, or its mean, is just the value itself:

$$\mathbb{E}\{\mathbf{Z}^*\} = \bar{\mathbf{Z}}^* + \mathbb{E}\{\alpha_x \mathbf{v}_1\} + \mathbb{E}\{\alpha_y \mathbf{v}_2\} = \bar{\mathbf{Z}}^* \quad (24)$$

Using Equations (21), (23) and (24) we can solve for the pointing vector error covariance.

$$\begin{aligned} P_{\mathbf{v}}^* &= \mathbb{E}\{(\mathbf{Z}^* - \bar{\mathbf{Z}}^*)(\mathbf{Z}^* - \bar{\mathbf{Z}}^*)^\top\} \\ &= \mathbb{E}\{(\alpha_x \mathbf{v}_1 + \alpha_y \mathbf{v}_2)(\alpha_x \mathbf{v}_1 + \alpha_y \mathbf{v}_2)^\top\} \\ &= \mathbb{E}\{\alpha_x^2 \mathbf{v}_1 \mathbf{v}_1^\top + \alpha_x \alpha_y \mathbf{v}_1 \mathbf{v}_2^\top + \alpha_y \alpha_x \mathbf{v}_2 \mathbf{v}_1^\top + \alpha_y^2 \mathbf{v}_2 \mathbf{v}_2^\top\} \\ &= \sigma_x^2 \mathbf{v}_1 \mathbf{v}_1^\top + \sigma_y^2 \mathbf{v}_2 \mathbf{v}_2^\top \end{aligned} \quad (25)$$

The main assumption made above is that the random variables α_x and α_y are uncorrelated. This is not required and this approach can be generalized should it be necessary to add cross correlation. As this is a bi-variate Gaussian distribution, a correlation coefficient between α_x and α_y is in essence a rotation of the uncertainty ellipsoid about its center. This same rotation can be achieved another way while still maintaining an uncorrelated α_x and α_y . Recall that during the set-up of the sensor-frame we performed an Euler 3-2 rotation sequence. If it was desired to rotate the ellipsoid in the sensor-frame, all one need do would be to perform a 3-2-1 rotation sequence instead where the angle of the third rotation about the X-axis is the desired angle by which we want to rotate the uncertainty ellipsoid. By introducing this third rotation there will be additional terms in $\hat{\lambda}$ and consequently $\mathbf{v}_1/\mathbf{v}_2$, however we can maintain that α_x and α_y are uncorrelated.

The above formulation for $P_{\mathbf{v}}^*$ is mathematically perfectly valid for a measurement corrupted by angular noise. However, because we have increased our measurement dimension from two to three, while only having uncertainty in two, the covariance matrix of our pointing vector is rank deficient. Rank-deficient matrices are undesirable for use within filtering algorithms. This is particularly due to the fact that mathematically it is not possible to invert a

rank-deficient matrix; a key operation in such algorithms. To circumvent this, we introduce an artificial uncertainty term along the direction in which there is no information to aid in numerical implementation. Recall that when deriving the rotation that described the sensor-frame, we made the active decision to align $\hat{\mathbf{X}}_S$ with the pointing vector $\bar{\mathbf{Z}}^*$. Inherent to this formulation is that $\mathbf{v}_1, \mathbf{v}_2$, and $\bar{\mathbf{Z}}^*$ make up an orthogonal space in \mathbb{R}^3 . Thus, $\bar{\mathbf{Z}}^*$ makes for a good axis to add this artificial noise to. This is done via the factor σ_{rng} and can be interpreted as the uncertainty in the length or distance of our pointing vector. With the artificial noise added in, the pointing error covariance is now of full rank.

$$\mathbf{P}_{\mathbf{v}}^* = \sigma_x^2 \mathbf{v}_1 \mathbf{v}_1^\top + \sigma_y^2 \mathbf{v}_2 \mathbf{v}_2^\top + \sigma_{\text{rng}}^2 \bar{\mathbf{Z}}^* \bar{\mathbf{Z}}^{*\top} \quad (26)$$

In Sections I and II.C.1 it was noted that the pointing vector covariance equation derived above generalizes the model proposed by Schuster[12] and expanded upon by Crassidis[13]. To show this, we must first assume the following.

- 1) The pointing vector is of unit length ($r = 1$)
- 2) There is no uncertainty in the length of the pointing vector ($\sigma_r = 0$)
- 3) The angular uncertainty is circular ($\sigma_x = \sigma_y$)

Under those assumptions, it can readily be shown that the pointing vector covariance reduces to the expression originally put forth by Schuster.

$$\begin{aligned} \mathbf{P}_{\mathbf{v}}^* &= \sigma_x^2 \begin{bmatrix} -c_\theta s_\phi \\ -s_\theta s_\phi \\ c_\phi \end{bmatrix} \begin{bmatrix} -c_\theta s_\phi & -s_\theta s_\phi & c_\phi \end{bmatrix} + \sigma_x^2 \begin{bmatrix} s_\theta \\ -c_\theta \\ 0 \end{bmatrix} \begin{bmatrix} s_\theta & -c_\theta & 0 \end{bmatrix} \\ &= \sigma_x^2 \begin{bmatrix} 1 - c_\theta^2 c_\phi^2 & -s_\theta c_\theta c_\phi^2 & -c_\theta s_\phi c_\phi \\ -s_\theta c_\theta c_\phi^2 & 1 - s_\theta^2 c_\phi^2 & -s_\theta s_\phi c_\phi \\ -c_\theta s_\phi c_\phi & -s_\theta s_\phi c_\phi & 1 - s_\phi^2 \end{bmatrix} \\ &= \sigma_x^2 (\mathbb{I}_{3 \times 3} - \bar{\mathbf{Z}}^* \bar{\mathbf{Z}}^{*\top}) \end{aligned} \quad (27)$$

Before moving on, it would be worthwhile to consider what the error covariance looks like in square-root (Cholesky) form and its inverse; for use within square-root and information filters. The Cholesky $\mathbf{S}_{\mathbf{v}}^*$ can be obtained by performing

a QR decomposition on the augmented matrix A .

$$P_v^* = AA^\top = S_v^* S_v^{*\top} \quad (28a)$$

$$A = \begin{bmatrix} \sigma_x \mathbf{v}_1 & \sigma_y \mathbf{v}_2 & \sigma_{\text{rng}} \tilde{\mathbf{Z}}^* \end{bmatrix} \quad (28b)$$

$$S_v^* = \text{qr}(A^\top, \text{"econ"})^\top \quad (28c)$$

In our case, the Cholesky is the upper square portion of the R matrix in the full QR decomposition. Recently it has become common for many programming languages to have an "economy" mode that produces this matrix directly.

Solving for the inverse of this matrix is not quite as simple. Let us first reformat the covariance to pull out the range uncertainty factor.

$$P_v^* = A^* A^{*\top} + \sigma_{\text{rng}}^2 \tilde{\mathbf{Z}}^* \tilde{\mathbf{Z}}^{*\top} \quad (29a)$$

$$A^* = \begin{bmatrix} \sigma_x \mathbf{v}_1 & \sigma_y \mathbf{v}_2 \end{bmatrix} \quad (29b)$$

To find the inverse, or technically the pseudo-inverse, we can implement what is known as the rank-1 update for the Moore-Penrose pseudo-inverse[29]. The generalized pseudo-inverse of a matrix $M \in \mathbb{R}^{m \times n}$, denoted M^\dagger , must satisfy

$$MM^\dagger M = M, \quad M^\dagger \in \mathbb{R}^{n \times m} \quad (30)$$

Here, because M need not be invertible, MM^\dagger is not necessarily the identity but does map the columns of M to itself.

In the case where M is invertible, the pseudo-inverse is equal to the inverse, $M^{-1} = M^\dagger$.

Returning to the problem at hand, applying the pseudo-inverse rank-1 update to the pointing vector error covariance in Equation (29a) gives

$$P_v^{*\dagger} = \left(A^* A^{*\top} + \sigma_{\text{rng}}^2 \tilde{\mathbf{Z}}^* \tilde{\mathbf{Z}}^{*\top} \right)^\dagger = \left(A^* A^{*\top} \right)^\dagger + G \quad (31)$$

where to solve for G , we must first evaluate the following intermediate terms.

$$\beta = 1 + \sigma_{\text{rng}}^2 \tilde{\mathbf{Z}}^{*\top} \left(A^* A^{*\top} \right)^\dagger \tilde{\mathbf{Z}}^* \quad (32a)$$

$$\mathbf{v} = \left(A^* A^{*\top} \right)^\dagger \sigma_{\text{rng}} \tilde{\mathbf{Z}}^* \quad (32b)$$

$$\mathbf{n} = \left(A^* A^{*\top} \right)^\dagger \sigma_{\text{rng}} \tilde{\mathbf{Z}}^* \quad (32c)$$

$$\mathbf{w} = \left(\mathbb{I} - \left(A^* A^{*\top} \right) \left(A^* A^{*\top} \right)^\dagger \right) \sigma_{\text{rng}} \tilde{\mathbf{Z}}^* \quad (32d)$$

$$\mathbf{m} = \left(\mathbb{I} - \left(A^* A^{*\top} \right)^\dagger \left(A^* A^{*\top} \right) \right) \sigma_{\text{rng}} \tilde{\mathbf{Z}}^* \quad (32e)$$

In order to simplify the equations above, a couple of identities from the PV derivation and the pseudo-inverse become useful: the formulation of the pointing vector necessitates that \mathbf{v}_1 , \mathbf{v}_2 , and $\bar{\mathbf{Z}}^*$ form an orthogonal basis, and for a general pseudo-inverse M^\dagger and M^\top share the same kernel (null space). With those rules established, the terms in Equation (32) simplify greatly to

$$\beta = 1, \quad \mathbf{v} = \mathbf{0}, \quad \mathbf{n} = \mathbf{0}, \quad \mathbf{w} = \sigma_{\text{rng}} \bar{\mathbf{Z}}^*, \quad \mathbf{m} = \sigma_{\text{rng}} \bar{\mathbf{Z}}^* \quad (33)$$

In our formulation of the PV covariance, $\|\mathbf{w}\|$ and $\|\mathbf{m}\|$ are necessarily not equal to zero. This is because $\|\bar{\mathbf{Z}}^*\| \neq 0$ and, as will be discussed in Section IV.C, $\sigma_{\text{rng}} \neq 0$. In the specific case where $\|\mathbf{w}\| \neq 0$ and $\|\mathbf{m}\| \neq 0$, we can express G as

$$G = -\frac{1}{\|\mathbf{w}\|^2} \mathbf{v} \mathbf{w}^\top - \frac{1}{\|\mathbf{m}\|^2} \mathbf{m} \mathbf{n}^\top + \frac{\beta}{\|\mathbf{m}\|^2 \|\mathbf{w}\|^2} \mathbf{m} \mathbf{w}^\top \quad (34)$$

Combining the terms from Equation (33) into Equation (34) yields the pointing vector covariance pseudo-inverse.

$$P_{\mathbf{v}}^{*\dagger} = \left(A^* A^{*\top} \right)^\dagger + G \quad (35a)$$

$$G = \frac{1}{\sigma_{\text{rng}}^2 r^2} \bar{\mathbf{Z}}^* \bar{\mathbf{Z}}^{*\top} \quad (35b)$$

IV. Implementation within Filtering Algorithms

As with many other precise orbit determination algorithms[3], an extended Kalman filter (EKF) is implemented using both the traditional azimuth and elevation formulation and the proposed pointing vector. Additionally, as will be discussed later in this section, the PV formulation lends itself well towards implementation within filters utilizing the information state such as the information EKF (EIF). The general EKF and EIF algorithms for continuous time non-linear dynamics with discrete non-linear measurements is outlined below.

A. Continuous-Discrete Extended Kalman Filter

The traditional algorithm for an EKF with continuous time dynamics and discrete time measurements can be broken down into two components. The first being the propagation step in which the prior state estimate and error covariance are propagated to the time of the measurement. The next component is the update step in which the propagated state and covariance are updated using received measurement.

1. System Dynamics and Measurement Model

First, we assume that the non-linear system dynamics and non-linear measurement model take the following general form.

$$\begin{aligned}\dot{\mathbf{X}} &= \mathbf{f}(\mathbf{X}, t) + B\mathbf{w} \\ \mathbf{Z}_k &= \mathbf{h}(\mathbf{X}_k) + \mathbf{v}_k\end{aligned}\tag{36}$$

Where \mathbf{X} is the state, $\mathbf{f}(\mathbf{X}, t)$ is the non-linear dynamics, B is the control mapping matrix, $\mathbf{w} \sim \mathcal{N}(0, P_{\mathbf{w}})$ is a random process noise term, \mathbf{Z}_k is the received measurement at time t_k , $\mathbf{h}(\mathbf{X})$ is the non-linear state-to-measurement mapping function, and $\mathbf{v}_k \sim \mathcal{N}(0, P_{\mathbf{v}})$ is a random measurement noise term.

2. Propagation Step

An underlying assumption when working with a POD algorithm such as an EKF is that there is at some prior time t_{k-1} an estimate of the state $\bar{\mathbf{X}}_{k-1}^+$ and error covariance P_{k-1}^+ available. In this notation a bar above a vector denotes that it is the estimate (mean) of that vector, a + as a superscript indicates that the value is evaluated after having received a measurement (a-posteriori), and the subscript of $k - 1$ means that this is all at time t_{k-1} . With the non-linear dynamical equations of motion available, the continuous-time propagation step consists of numerically integrating the state estimate mean ($\bar{\mathbf{X}}$) and error covariance (P) from the prior time t_{k-1} , with initial conditions $\bar{\mathbf{X}}(t_{k-1}) = \bar{\mathbf{X}}_{k-1}^+$ and $P(t_{k-1}) = P_{k-1}^+$, to the current time t_k according to the following first order differential equations.

$$\begin{aligned}\dot{\bar{\mathbf{X}}} &= \mathbf{f}(\bar{\mathbf{X}}, t) \\ \dot{P} &= F(\bar{\mathbf{X}}, t)P^\top + PF(\bar{\mathbf{X}}, t)^\top + BP_{\mathbf{w}}B^\top \\ F(\bar{\mathbf{X}}, t) &= \left. \frac{\partial \mathbf{f}}{\partial \mathbf{X}} \right|_{\bar{\mathbf{X}}}\end{aligned}\tag{37}$$

This yields the propagated state estimate $\bar{\mathbf{X}}_k^-$ and error covariance P_k^- at time t_k prior to the measurement update, noted with the $-$ in the superscript (a-priori).

3. Update Step

Once a state estimate and error covariance at the current time have been obtained, we can use the received measurement to update said values. First, a handful of gain matrices must first be established.

$$\begin{aligned}W_k &= H_k(\bar{\mathbf{X}}_k^-)P_k^-H_k(\bar{\mathbf{X}}_k^-)^\top + P_{\mathbf{v}} \\ C_k &= P_k^-H_k(\bar{\mathbf{X}}_k^-)^\top \\ K_k &= C_kW_k^{-1} \\ H(\bar{\mathbf{X}}) &= \left. \frac{\partial \mathbf{h}}{\partial \mathbf{X}} \right|_{\bar{\mathbf{X}}}\end{aligned}\tag{38}$$

Here W_k is the measurement residual $(\mathbf{Z}_k - \bar{\mathbf{Z}}_k)$ covariance matrix, C_k is the a-priori state and measurement residual cross-covariance, and K_k is the optimal Kalman gain. With these values established the EKF update step is given as

$$\begin{aligned}\bar{\mathbf{X}}_k^+ &= \bar{\mathbf{X}}_k^- + K_k (\mathbf{Z}_k - \mathbf{h}(\bar{\mathbf{X}}_k^-)) \\ P_k^+ &= P_k^- - C_k K_k^\top - K_k C_k^\top + K_k W_k K_k^\top\end{aligned}\tag{39}$$

The propagation and measurement update steps are then repeated iteratively throughout the trajectory to obtain an estimated trajectory and linear error covariance history

4. Underweighting

Within POD algorithms such as an EKF, a common issue encountered is divergence due to large measurement residuals. This is primarily due to the measurement linearization in the update step. As the measurement residual increases, the linearized approximation of the state-to-measurement mapping function breaks down, leading to potentially large and inaccurate updates. A widely adopted "band-aid" for this is to implement what is often referred to as underweighting or damping[7]. An underweighted Kalman filter examines the difference between the actual measurement covariance and the predicted measurement covariance, via the linearized state-to-measurement function, and lessens the update if that difference exceeds some relative value. This is in essence, a comparison between the confidence in state and the confidence in measurement:

$$\text{tr}(H_k P_k^- H_k^\top) > \frac{p}{1-p} \text{tr}(P_v)\tag{40}$$

Here p is a tuning parameter that increases or decreases the tolerance for performing the Kalman gain underweighting. Unfortunately, this inequality is not well suited for implementation with the pointing vector. As will be discussed in Section IV.C, the PV error covariance has arbitrarily large uncertainty values along the directions in which there is no information. Because of this, the policy in Equation (40) is rarely ever met. Alternatively, if we work within the information space, the inverse of the covariance matrices, we can analytically represent the infinite uncertainty as zero and make a more direct comparison.

$$\text{tr}(H_k (P_k^-)^{-1} H_k) < \frac{1-p}{p} \text{tr}(P_v^{-1})\tag{41}$$

While these two inequalities are not analytically equivalent, they serve the same purpose and can similarly be tuned via the choice of p . Checked during each measurement update, if either of the inequalities above are met, the Kalman gain

is reduced and the update continues as before.

$$\begin{aligned} W_k &= \frac{1}{p} H_k(\bar{\mathbf{X}}_k^-) P_k^- H_k(\bar{\mathbf{X}}_k^-)^\top + P_v \\ K_k &= C_k W_k^{-1} \end{aligned} \quad (42)$$

A value of $p = 1$ corresponds to a linearly optimal filter.

B. Information State Extended Kalman Filter

As will be discussed later in this section, the pointing vector measurement formulation is particularly well suited for implementation within what is known as the information EKF. While mathematically identical to the traditional EKF, the information filter works with the information state \mathbf{Y} and matrix Λ .

$$\begin{aligned} \mathbf{Y} &= \Lambda \mathbf{X} \\ \Lambda &= P^{-1} \end{aligned} \quad (43)$$

The state dynamics and measurement model are assumed to take the same form as in Equation (36).

1. Propagation Step

Just as was done in with the EKF, the propagation step consists of integrating the information state ($\bar{\mathbf{Y}}$) and matrix (Λ) from the prior time t_{k-1} , with initial conditions $\bar{\mathbf{Y}}(t_{k-1}) = \bar{\mathbf{Y}}_{k-1}^+$ and $\Lambda(t_{k-1}) = \Lambda_{k-1}^+$, to the current time t_k according to the following first order differential equations.

$$\begin{aligned} \dot{\bar{\mathbf{Y}}} &= \dot{\Lambda} \Lambda^{-1} \bar{\mathbf{Y}} + \Lambda \mathbf{f}(\bar{\mathbf{X}}, t) \\ \dot{\Lambda} &= \Lambda F(\bar{\mathbf{X}}, t) + F(\bar{\mathbf{X}}, t)^\top \Lambda + \Lambda B P_w B^\top \Lambda \end{aligned} \quad (44)$$

However, because the dynamics are a function of the state directly, we must continually solve the transform given in Equation (43) to perform the above integration. The result will be the a-priori information state $\bar{\mathbf{Y}}_k^-$ and matrix Λ_k^- .

2. Update Step

The measurement update step of the information EKF is computationally much lighter and given below.

$$\begin{aligned} \bar{\mathbf{Y}}_k^+ &= \bar{\mathbf{Y}}_k^- + H_k(\bar{\mathbf{X}}_k^-)^\top P_v^{-1} (H_k(\bar{\mathbf{X}}_k^-) \bar{\mathbf{X}}_k^- + \mathbf{Z}_k - \mathbf{h}(\bar{\mathbf{X}}_k^-)) \\ \Lambda_k^+ &= \Lambda_k^- + H_k(\bar{\mathbf{X}}_k^-)^\top P_v^{-1} H_k(\bar{\mathbf{X}}_k^-) \end{aligned} \quad (45)$$

This is primarily due to the fact that there is no large inverse to take like there was in the EKF.

The information state EKF is particularly useful for a number of reasons. First, the information matrix (covariance

inverse) is much more well suited towards handling particularly large, or small, variances. This may be useful during filter initialization as it can allow the designer to set the initial information matrix to zero, an infinite covariance matrix. Another advantage to the information matrix is that it directly works with the inverse of the measurement error covariance. This specific property will be exploited in later sections for use with the pointing vector specifically.

C. State to Pseudo-Measurement Mapping

In the proposed measurement model, there is still the matter of the scalar length by which the pointing vector is multiplied. Depending on the measurement model of interest (e.g. angles-only, range-only, angles+range), the approach will be slightly different.

1. Angles Only

For the case where angles-only measurements are available, let us strategically choose r to be the expected distance of the spacecraft from the observer. Recall that \mathbf{Z}_k is the received noisy azimuth and elevation measurement and \mathbf{Z}_k^* is the pointing vector pseudo-measurement used within the filter.

$$\mathbf{Z}_k = \begin{bmatrix} \theta \\ \phi \end{bmatrix} \quad (46a)$$

$$\mathbf{Z}_k^* = \mathbf{g}^*(\mathbf{Z}_k, \bar{\mathbf{X}}_k^-) = \bar{r}_{\text{rel}} \begin{bmatrix} C_\phi C_\theta \\ C_\phi S_\theta \\ S_\phi \end{bmatrix} \quad (46b)$$

$$\bar{r}_{\text{rel}} = \|\bar{\mathbf{r}}_k^- - \mathbf{r}_O\| \quad (46c)$$

This choice of r allows the state-to-pseudo-measurement mapping function $\mathbf{h}^*(\bar{\mathbf{X}}_k^-)$ to become linear in state. However, this implies that to compute the pointing vector, one must use the actual measured azimuth and elevation, as well as the predicted state value for that time step. This value for r is also used in calculating the pointing vector covariance.

By letting r be equal to the expected distance, we can express the state-to-measurement equation used within the filter as a linear operator

$$\mathbf{h}^*(\bar{\mathbf{X}}_k^-) = \begin{bmatrix} \mathbb{I}_{3 \times 3} & \mathbf{0}_{3 \times 3} \end{bmatrix} \bar{\mathbf{X}}_k^- - \mathbf{r}_O \quad (47)$$

And thus the measurement Jacobian used is constant and exactly:

$$H_k^*(\bar{\mathbf{X}}_k^-) = \begin{bmatrix} \mathbb{I}_{3 \times 3} & \mathbf{0}_{3 \times 3} \end{bmatrix} \quad (48)$$

A linear measurement model is great, however this suggests that we have some information about the position in three orthogonal directions. As we can only measure the azimuth and elevation we have no knowledge of the distance. Here the artificial noise scaling factor σ_{rng} mentioned earlier becomes helpful. Setting this value to a large number implies that there is little information in the range of the spacecraft from the observer. This value can be used as a tuning parameter and has been found to perform well when the scale factor is roughly five orders of magnitude larger than the angular uncertainty, that is $\sigma_{\text{rng}} = 10^5 \sigma_{x,y}$. Letting it be a function of the known angular uncertainty aids in maintaining a covariance matrix that is well-scaled for a variety of σ_x and σ_y .

In effect, the uncertainty in the range is infinite. If we are working within traditional filters, this is mathematically impractical to represent without saturating the covariance matrix. Alternatively, using a value of infinity for σ_{rng} in the pseudo-inverse formulation in Equation (35) causes G to drop nicely to zero. This allows for the pointing vector to be implemented within information filters directly and without the need for tuning.

2. Range Only

In the case where range is the only measurement available, we perform a very similar procedure but with the measured and expected values reversed. Here, with a relative range measurement (and error uncertainty) provided, we use our state estimate to determine the expected azimuth and elevation values.

$$Z_k = r_{\text{rel}} + \mathcal{N}(0, \sigma_{\text{rng}}) \quad (49a)$$

$$\mathbf{Z}_k^* = \mathbf{g}^*(Z_k, \bar{\mathbf{X}}_k^-) = Z_k \begin{bmatrix} C_{\bar{\phi}} C_{\bar{\theta}} \\ C_{\bar{\phi}} S_{\bar{\theta}} \\ S_{\bar{\phi}} \end{bmatrix} \quad (49b)$$

$$\bar{\theta} = \tan^{-1} \left(\frac{\bar{y}_k^- - y_O}{\bar{x}_k^- - x_O} \right) \quad (49c)$$

$$\bar{\phi} = \sin^{-1} \left(\frac{\bar{z}_k^- - z_O}{\|\bar{\mathbf{r}}_k^- - \mathbf{r}_O\|} \right) \quad (49d)$$

Just as we did with the angles-only measurements, we use the expected azimuth and elevation values $(\bar{\theta}, \bar{\phi})$ along with the measured range ($Z_k = r_{\text{rel}}$) within our covariance expression Equation (26). However, in this situation our range uncertainty (σ_{rng}) is known from the sensor specifications and the angular uncertainty is theoretically infinite. In practice, a value five orders of magnitude larger than the range uncertainty has worked well ($\sigma_x = \sigma_y = 10^5 \sigma_{\text{rng}}$). Due to the formulation of the pointing vector, the state-to-measurement mapping function will remain the same as the one used for the angles-only measurements.

3. Angles and Range

For the case when both range and angular measurements are available, we simply combine the above two methods. Using our measured values along with their associated uncertainty, we can fully characterize the measurements via the linear pointing vector model, and with information in 3 orthogonal directions.

$$\mathbf{Z}_k = \begin{bmatrix} r_{\text{rel}} \\ \theta \\ \phi \end{bmatrix} \quad (50)$$

$$\mathbf{Z}_k^* = \mathbf{g}^*(\mathbf{Z}_k) = r_{\text{rel}} \begin{bmatrix} C_\phi C_\theta \\ C_\phi S_\theta \\ S_\phi \end{bmatrix}$$

V. Simulation Results

Analysis of the proposed pointing vector will be completed within a cis-lunar object tracking scenario. As discussed throughout Sections III and IV, the pointing vector is most suited towards the case of angles-only measurements. As such, the majority of the simulations and corresponding analysis will focus on a number of scenarios involving optically based angles-only tracking. However, a couple of additional cases will be presented to show the validity of the range-only measurements and the fusion of range and angle measurements. To ensure repeatability, the spacecraft will be in one of four periodic orbits within the CR3BP Earth-Moon system: an L1 northern halo orbit (NHO), L2 southern halo orbit (SHO), L2 southern near-rectilinear halo orbit (S-NRHO), and an L1 Lyapunov orbit. The individual trajectories can be seen in Figure 5 and the specific SC initial conditions and observer locations can be seen in Table 1. Additionally, as this comparison is meant to test the limit of each measurement formulation, the initial spacecraft position in each of these orbits and the orientation of the sensor is chosen to minimize the time that the spacecraft is visible to the observer.

Table 1 Spacecraft Initial State and Observer Location

Spacecraft State Initial Conditions				
	L1 NHO	L2 SHO	L2 S-NRHO	L1 Lyap
x_0	0.8667	1.0870	0.9872	0.9136
y_0	-0.1062	-0.1310	-0.0006	0.0004
z_0	0.1162	-0.0867	0.0128	0
\dot{x}_0	-0.1032	-0.1056	-0.0027	-0.0009
\dot{y}_0	0.1644	-0.0635	1.3468	-0.4870
\dot{z}_0	0.1856	0.2072	0.0305	0
Obs Loc	-Z	+Y	+Y	-Y

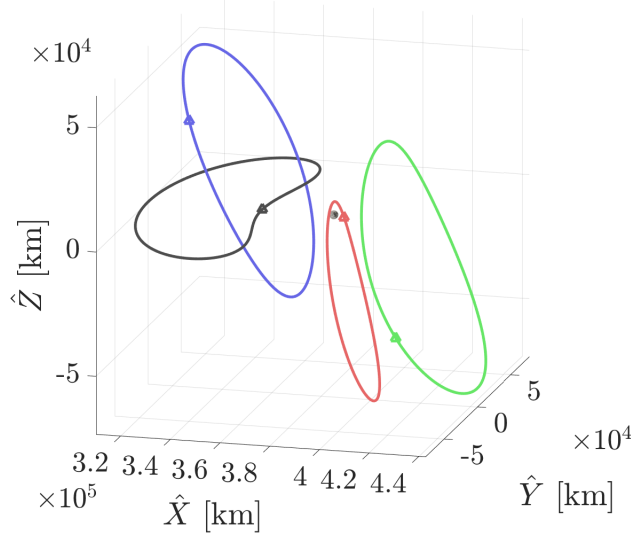


Fig. 5 3D Spacecraft Trajectories

A. Angles Only

Analysis of the angles-only measurements is done by running identical tracking scenarios of a spacecraft in an orbit near the Moon but in one case using the traditional azimuth/elevation measurements in an EKF, in another case using the pointing vector in an EKF, and in a third case using pointing vector but in an information EKF.

As mentioned, the initial orbit conditions and sensor locations were intentionally selected to yield large intervals of time in which there are no measurements and in which there is an initial period of 5-10 days of propagation before the first measurement becomes available. In such test cases, the performance of the linearized measurement equations for azimuth and elevation become the leading source of filter divergence. Large occlusion intervals like this are not particularly uncommon in practice. One example might be from the perspective of multi-object tracking and space-domain awareness. If we can extend the time in between measurements before a filter breaks down and diverges, that time can be spent on collecting measurements of other objects, thus increasing the total number that can be tracked. Similarly, there are many situations in which we are forced into not taking a measurement for long periods of time. Such a case might arise if one is trying to track a spacecraft in a high altitude orbit that only becomes viewable for a few hours every couple days.

1. Baseline Filter Results

For the measurement comparison, three Monte-Carlo trials will be run for each orbit/sensor case: one implementing the traditional azimuth/elevation in an EKF, another using the proposed pointing vector in an EKF, and lastly the pointing vector in an information EKF. For each of these cases the baseline filter parameters, also inspired by Ref. 18, are outlined in Table 2. Importantly, for the baseline filter, a significant amount of process noise is used to account for any unmodeled acceleration. Comparatively, in the Earth-Moon regime, accelerations of this magnitude are similar if

not slightly larger than those attributed to solar radiation pressure (SRP)[30].

Table 2 Baseline Filter Parameters

Initial Position S.D. [km]	50
Initial Velocity S.D. [km/s]	10^{-3}
Measurement Noise S.D. ($\sigma_\theta = \sigma_\phi = \sigma_x = \sigma_y$) [deg]	10^{-3}
Range Uncertainty S.D. (σ_{rng}) [km]	10^5
Process Noise S.D. (σ_{acc}) [$\frac{\text{km}}{\text{s}^2}$]	10^{-8}
Measurement Interval [min]	30
Field of Regard ($\psi_{\text{FoR,lim}}$) [deg]	70
Simulation Time [days]	40
Filter Damping Ratio (p) [N/A]	1 (optimal)

The Monte-Carlo runs for the baseline filter parameters can be seen for each configuration in Figure 6. As to not take up more space with error plots, the information EKF plots for the pointing vector are omitted as they are broadly reflective of their normal EKF counterpart. The columns of Figure 6 correspond to simulations implementing the same measurement type, while the rows correspond to simulations with the same SC orbit/sensor configuration. The first three plots of each correspond to the position errors where the colored lines represent the trials in which the EKF successfully converged, the transparent gray lines to the trials that did not converge, and the dotted lines represent the filter's predicted three sigma bounds. Additionally, the plot at the bottom of each shows whether or not the spacecraft was visible at that time. Table 3 shows the convergence characteristics for each case.

In all configurations the traditional azimuth/elevation formulation fails to converge robustly. On the other hand, the pointing vector formulation converges roughly 95% of the time or more. It should also be noted that the information EKF using the pointing vector has identical convergence characteristics to the normal EKF. As is demonstrated, the proposed pointing vector formulation performs substantially better than simply using azimuth and elevation in an untuned, optimal EKF. As was mentioned, this analysis was inspired by Ref. 18 and as such, we can compare our results and better evaluate how this method stacks up to more complex algorithms such as the GM-EKF. First, our pointing vector results including the 3σ bounds and error magnitudes are consistent with the observable cases presented in Ref. 18. Furthermore, the orbit initial conditions and sensor locations used in this study, with azimuth/elevation measurements, displayed similar divergence characteristics to those in Ref. 18. For these cases, Ref. 18 found that a GM-EKF was necessary to prevent filter divergence. However, with the proposed pointing vector formulation we see a substantial increase in convergence with a plain Gaussian filter and no tuning. To aid with the physical intuition of the filter performance, Figure 7 shows the trajectory estimates for the L2 S-NRHO case.

Importantly, as this approach is a simple measurement reformulation, it would be completely feasible to implement the pointing vector measurement into a more advanced filtering algorithm such as a GM-EKF. When combined one would get the advantages of a linear measurement function, along with the advantages that a GMM provides such as its

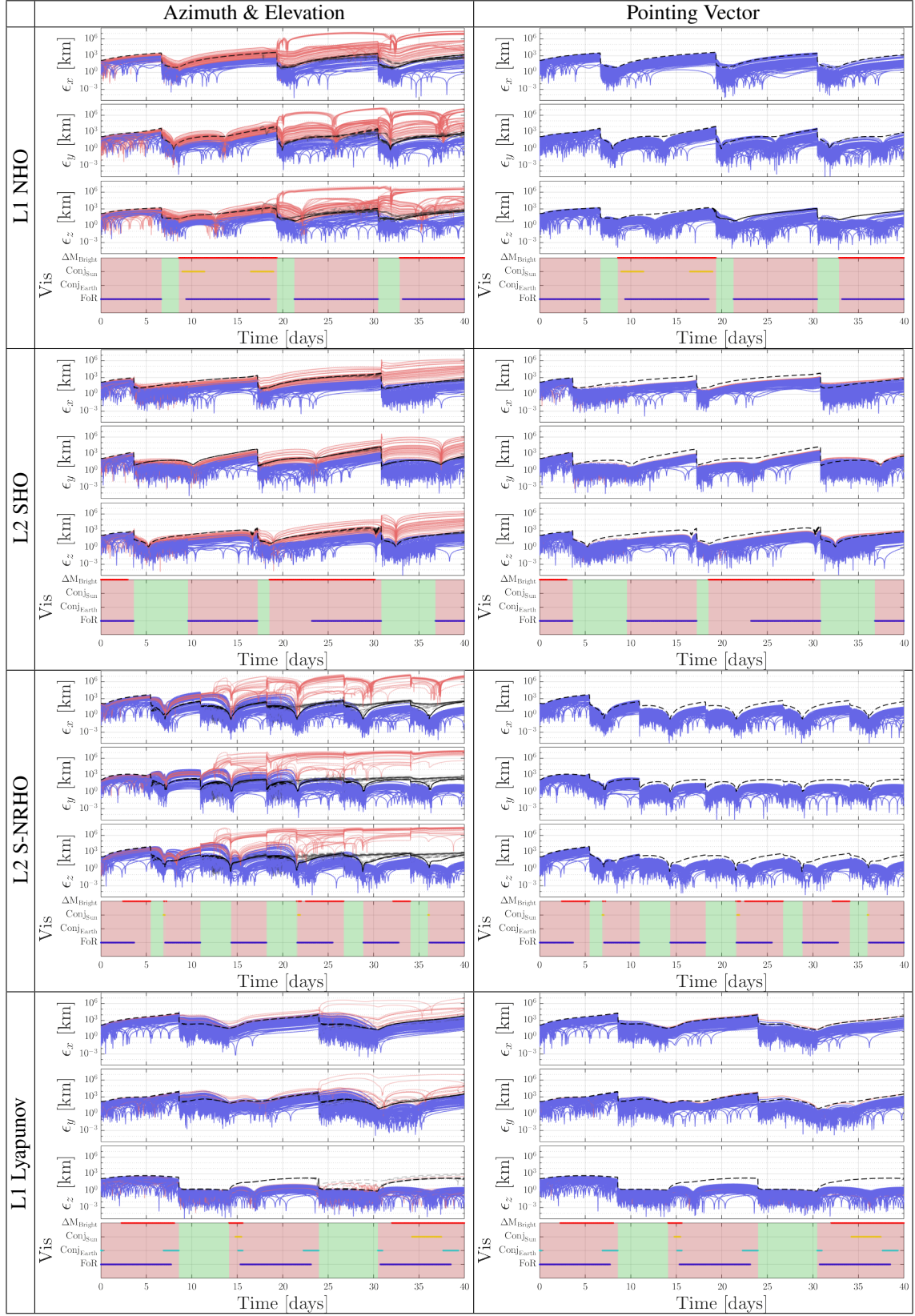


Fig. 6 Baseline Angles-Only EKF Monte Carlo Position Errors

Table 3 Baseline EKF Results: Angles-Only Trial Convergence out of 100 Samples

Measurement Type	Orbit Configuration			
	L1 NHO	L2 SHO	L2 SNRHO	L1 Lyap
Azimuth/Elevation	34	62	71	88
Pointing Vector	100	94	100	98
Information - Pointing Vector	100	94	100	98

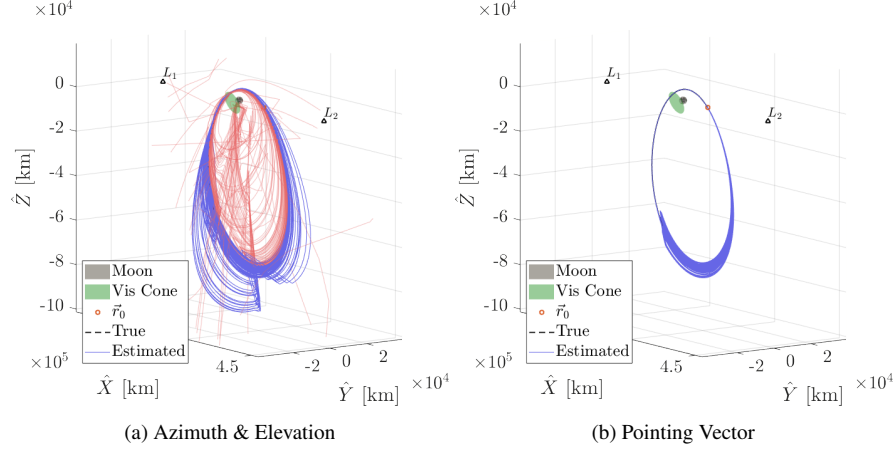


Fig. 7 L2 Southern NRHO Angles-Only Baseline Filter Monte-Carlo Trajectory Estimates

non-linear, non-Gaussian dynamics propagation.

A closer inspection into the most difficult scenarios can provide some further insight as to the advantages of the pointing vector formulation. The L1 Northern halo orbit and the L2 Southern halo orbit proved to be the most difficult for the filters. Both of these cases exhibit observational windows where the SC is obscured longer than it is visible. Also, of the trajectories examined, the L1 NHO and L2 SHO are on average the furthest from the observer. This is evident in that the SC is too dim with respect to the background sky for longer portions of its orbit. These two cases will be explored further in the next section using a fine-tuned EKF. Another vital reason why these two cases are particularly difficult has to do with their linear stability within the CR3BP system. Both the L1 NHO and L2 SHO are quite unstable causing them to diverge quickly from their periodic orbit when perturbed. In filtering terms, this causes the covariance matrix to grow rapidly when propagating.

2. Tuned Filter Results

Up to this point all simulations and results have implemented the optimal form of the EKF. As discussed, it is well known that the traditional EKF can encounter filter divergence issues especially when working with highly non-linear measurements such as azimuth and elevation. To further examine the performance of the proposed measurement formulation, we repeat the two most difficult simulations but using a fine-tuned filter for the azimuth and elevation measurements and an un-tuned filter, with decreased process noise, for the pointing vector. For this study it was found

that a value of $p = 0.75$ worked well for the damping ratio used in Equation (40), when implemented for the traditional azimuth and elevation filter. Alternatively, attempting to underweight the angles-only EKF implementing the pointing vector measurement had little impact on performance. Lastly, a smaller process noise of $\sigma_{acc} = 10^{-9} \left[\frac{\text{km}}{\text{s}^2} \right]$ is used for both filters.

It is not immediately apparent why the pointing vector formulation appears to be unchanged when implementing an underweighted filter. For this we return to the original motivation behind underweighting. Inherent to the EKF is a linearized measurement function. As the measurement residual increases not only does this linear approximation break down, but so to does the calculated measurement Jacobian. However, from the perspective of the EKF the pointing vector measurement is a linear function of the state variable. This is why underweighting seems to have little effect on the performance of filters that implement the pointing vector measurement. Table 4 gives a breakdown of the number of converged trials as well as the position RMSE, averaged across one period of the orbit at the end of the simulation. In the calculation of the RMSE, all trials that resulted in a divergent filter were discarded.

Table 4 Fine-Tuned EKF Results: Angles-Only Trial Convergence and Position RMSE

Measurement Type	L1 NHO		L2 SHO	
	# Trials Converged	Position RMSE [km]	# Trials Converged	Position RMSE [km]
Azimuth/Elevation	94	18.9420	99	39.2234
Pointing Vector	94	19.3152	99	30.2418
Information - Pointing Vector	94	19.3152	99	30.2418

With this, we can further appreciate the power of the pointing vector formulation. First, it took considerable underweighting to allow for the azimuth/elevation filter to perform similarly to the untuned pointing vector. Conversely, the pointing vector filter maintained good convergence characteristics while still being able to handle the reduced amount of process noise. It should also be noted that the pointing vector formulation generally results in a smaller RMSE. Figure 8 gives a similar showing of the position estimate errors but with the revised filter parameters. This shows graphically what was observed in Table 4. The azimuth/elevation filter can be underweighted to converge more robustly and with less error but not to exceed the untuned pointing vector.

As noted earlier, large measurement residuals can be a leading cause of filter divergence especially with highly non-linear measurement functions. This is one of the more likely causes of the poor convergence characteristics observed in left most columns of Figures 6 and 8. Alternatively, because the pointing vector is formulated to be a linear transform of the state variable, there is no loss in the measurement equation when dealing with large residuals. Instead, the linearization takes place in the characterization of the measurement error in the covariance matrix. This was the small angle approximation described earlier in Equation (18). When working with angular uncertainties on the order of a degree or less, the small angle approximation holds quite well. Because this linearization occurs within the covariance

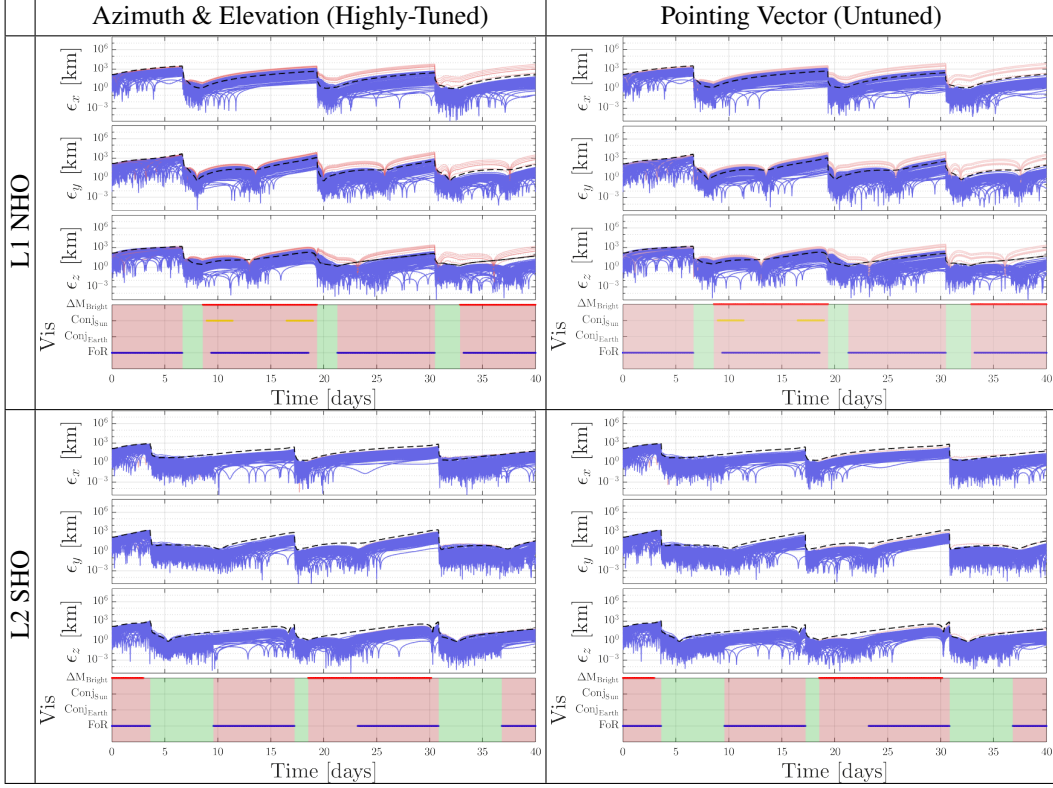


Fig. 8 Highly Challenging Scenarios: Angles-Only Tuned Filter Monte Carlo Position Errors

matrix, the impact of large residuals is much reduced.

Lastly, it is important to reiterate that this approach still assumes that the received measurements are the azimuth and elevation. However, instead of working with those angles directly inside the filter, a pointing vector and associated covariance is calculated that eliminates the non-linearity in the measurement function while more accurately describing the angular uncertainty associated with line of sight measurements.

B. Range Only

For the application of the pointing vector to range-only measurements we consider just two test scenarios. The L2 southern NRHO and the L1 Lyapunov orbit are chosen as they are representative of near marginally-stable and unstable orbits within the CR3BP system. For this case, it was found that the induced linearity of the pointing vector was not as strong as in the angles-only case. To improve the performance, underweighting is similarly applied to the pointing vector EKF but using the inverse policy outlined in Equation (41). This analysis is completed using similarly tuned filters and the baseline parameters presented in Table 2. Seeing as we are now directly measuring the relative range, the distance uncertainty is chosen to be $\sigma_{\text{rng}} = 50$ [m] both for measurement generation and within the pointing vector formula. Consequently, the angular uncertainty is technically infinite but is chosen to be $\sigma_x = \sigma_y = 10^5 \sigma_{\text{rng}}$. This is the reverse of what was done for the case of angles-only measurements. The results of these simulations are provided

through Monte Carlo error plots similar to the previous sections in Figure 9.

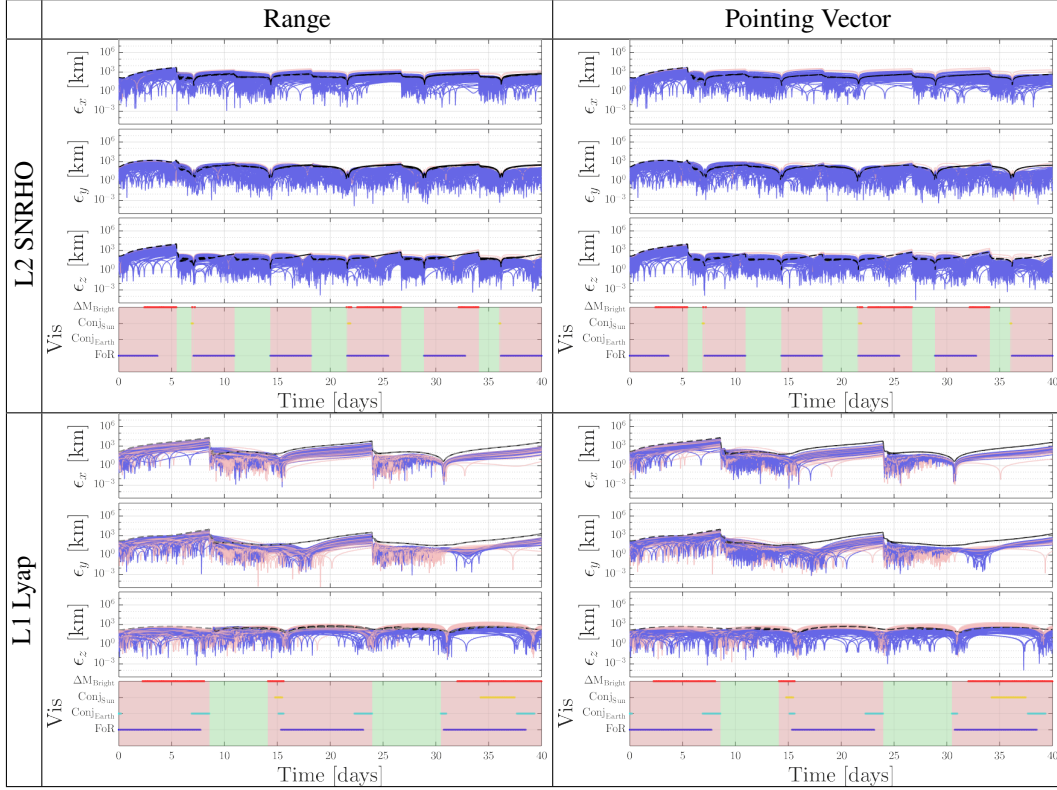


Fig. 9 Range-Only Filter Monte Carlo Position Error

Table 5 Range Only EKF Results: Trial Convergence and Position RMSE

Measurement Type	L2 SNRHO		L1 Lyap	
	# Trials Converged	Position RMSE [km]	# Trials Converged	Position RMSE [km]
Range	98	113.029	47	193.118
Pointing Vector	98	103.191	52	157.579

Interestingly, the pointing vector yielded very little increase in performance over the traditional range-only formulation. From Table 5 we see that there is a small performance increase the convergence rate of the pointing vector filter, accompanied by a slight decrease in RMSE values, however the difference is considerably less than those associated with the angles-only filters. There are two possible reasons for such ambiguity that are immediately apparent. First, the traditional range formulation, the norm of the relative position, has a first order Taylor-series approximation that is much more well behaved in comparison to the azimuth and elevation case. The second possibility is that strictly range-only measurements contain so little state information that any reformulations of the measurement can inherently add error due to the unique numerical processes used in the implementation of each.

C. Range and Angles

When applied to the fusion of range and angles the pointing vector is fully characterized. Because the error covariance is of full rank, the case the PV measurement formulation can be directly implemented within an EKF without approximation. Using the same sensor and filter initialization parameters as outlined in Sections V.A.1 and V.B the range+angles filter is implemented for just the L2 S-NRHO to demonstrate feasibility. Figure 10 shows the results as a collection of 3D estimated trajectories and the individual position errors and associated 3σ bounds.

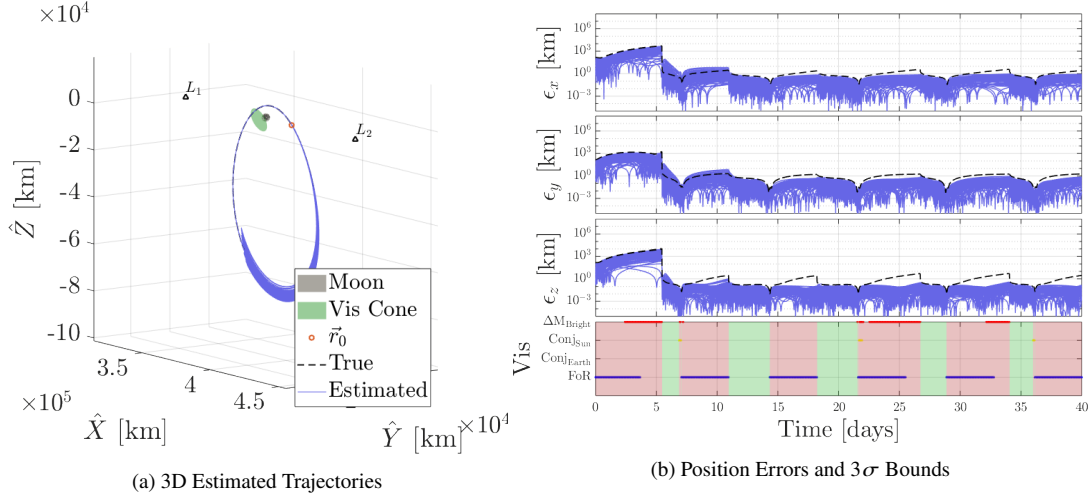


Fig. 10 Range+Angles, L2 S-NRHO, EKF Tracking Results

Comparing these results with those from Figures 6 and 9 reveals that, as expected, the filter receiving both range and angular measurements performs substantially better than those implementing either measurement alone. Though not a thorough study of range and angle measurement fusion, this result is promising and illustrates the feasibility of using the pointing vector formulation for situations in which both measurements are available.

D. Discussion

A recurring concern when developing a simulation to test a filter is ensuring that there is no additional information or truth knowledge that the filter is fed other than the noisy measurements and a set of randomly sampled initial conditions. Throughout the derivation of the pointing vector, the use of existing state knowledge to augment the received measurement was initially a source of concern. To ensure that the proposed formulation did not misrepresent the actual information available, it is useful to consider the best case performance of these filters. For this we can implement the Cramer-Rao lower bound (CRLB) for deterministic systems[31]. For our cases, this essentially consists of propagating the covariance with zero process noise when the SC is not visible, and performing the optimal form of the update step when a measurement is available. Figure 11 shows the covariance CRLBs for two cases implementing angles-only measurements.

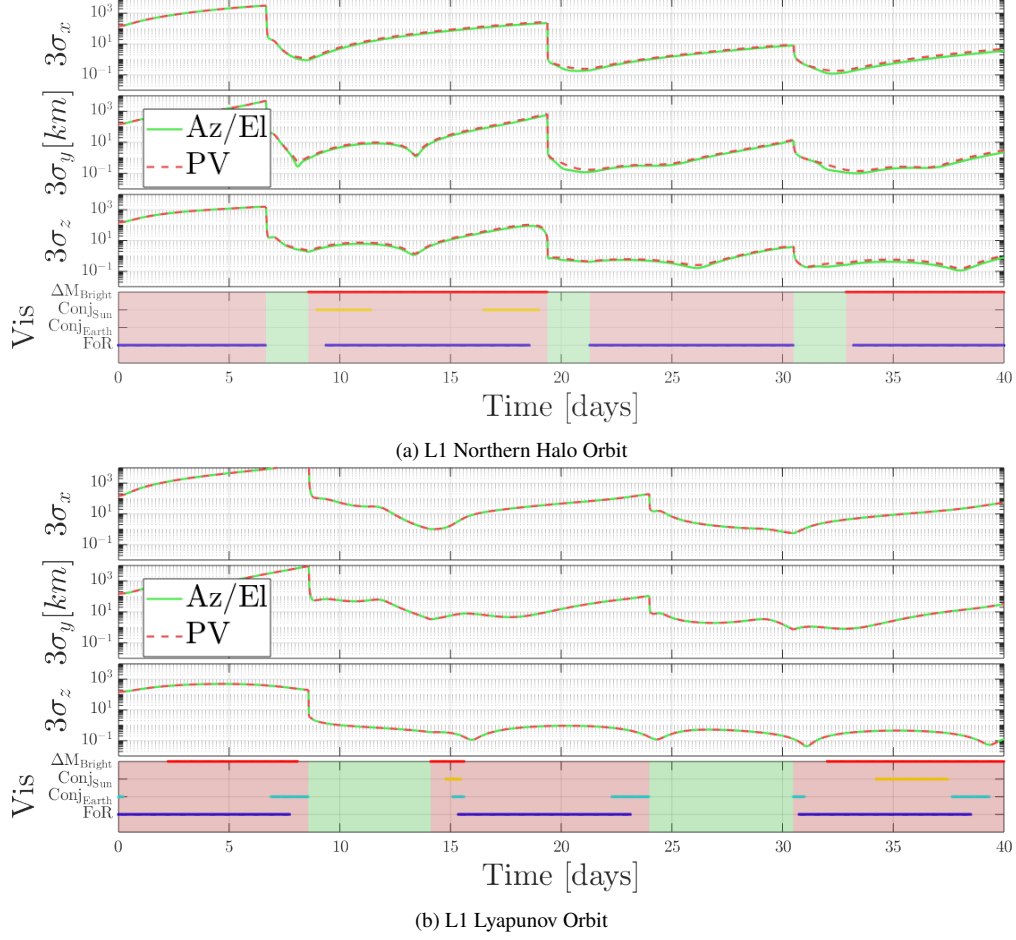


Fig. 11 3σ Position Cramer-Rao Lower Bounds for Baseline Filter

As demonstrated, the theoretical minimum of the covariance for the baseline filters are nearly identical. This suggests that though we have constructed an alternate way to integrate our angular measurements into the filter, the fundamental information being added is the same. Curiously, for the case of the L1 Lyapunov orbit, the CRLB plots are not only similar but truly identical. This can be attributed to the L1 Lyapunov orbit being a purely planar orbit and the sensor lying in said plane. This results in the elevation measurement, without noise, always being zero. In this case, the measurement noise pdf generated by assuming uncorrelated white Gaussian noise for azimuth and elevation (Equation (4)) is the same as the noise pdf generated via the pointing vector rotation (Equations (21) and (22)). Geometrically this can be intuited by considering azimuth and elevation as the longitude and latitude lines on the globe. At the equator (zero elevation) the longitude lines are parallel and the latitude lines look straight. However, as we increase or decrease our elevation, the longitude lines stop being parallel until they intersect at the pole. This is why in the 3D orbit cases, as shown in Figure 11(a), the CRLB of the filter implementing azimuth and elevation is slightly smaller than that of the pointing vector.

VI. Conclusions

This paper proposes an alternative measurement formulation that can be applied to angles-only, range-only, and range+angles navigation and object tracking. Specifically, the results presented in this paper show that in the case of angles-only measurements, the proposed pointing vector has significantly better convergence and error characteristics. By converting commonly received azimuth and elevation measurements into a linear transform of the state variable, and properly modeling the linear state error to geometrically match that of the non-linear measurement, one can significantly improve the performance, and robustness of their filtering algorithm. When tracking an object in cis-lunar space with infrequent measurements, the pointing vector formulation resulted in a filter convergence rate of over 94%. Conversely, filters using the traditional azimuth and elevation had a convergence rate of on average $\approx 65\%$ when applied to identical scenarios. Furthermore, due to the pointing vector taking on a linear form with respect to the state, smaller amounts of process noise can be used without impacting convergence. The pointing vector measurement model, due to its unique formulation, is perfectly situated to be implemented within information state filters. This allows the user to virtually eliminate the need for further tuning that is often needed within traditional filters. As is demonstrated throughout, this paper suggests that a simple reformulation of highly non-linear measurement, such as azimuth and elevation, into a linear transform of the state can substantially increase the performance characteristics of a navigation or tracking algorithm.

References

- [1] Kepler, J., and Brahe, T., *Astronomia Nova Aitiologetos*, 1st ed., G. Voegelinus, Paris, France, 1609.
- [2] Mulrooney, M., Hickson, P., Stansbery, E., and Barker, E., “Orbital Debris Detection and Tracking Strategies for the NASA/AFRL Meter Class Autonomous Telescope (MCAT),” *61st International Astronautical Congress*, International Astronautical Federation, Prague, Czech Republic, 2010, p. 10.
- [3] Tapley, B. D., Schutz, B. E., and Born, G. H., *Statistical Orbit Determination*, 1st ed., Elsevier Academic Press, 2004.
- [4] Iannamorelli, J. L., and LeGrand, K. A., “Adaptive Gaussian Mixture Filtering for Multi-Sensor Maneuvering Cislunar Space Object Tracking,” *Journal of Astronautical Sciences*, Vol. in press, 2024.
- [5] LeGrand, K. A., Khilnani, A. V., and Iannamorelli, J. L., “BAYESIAN ANGLES-ONLY CISLUNAR SPACE OBJECT TRACKING,” *33rd AAS/AIAA Space Flight Mechanics Meeting*, American Astronomical Society, Austin, TX, 2023.
- [6] Greaves, J. A., and Scheeres, D. J., “Relative Estimation in the Cislunar Regime using Optical Sensors,” *Advanced Maui Optical and Space Surveillance Technologies Conference*, Advanced Maui Optical and Space Surveillance Technologies, Maui, HI, 2021, p. 21.
- [7] Carpenter, J. R., and D’Souza, C. N., “Navigation Filter Best Practices,” Technical Report 2018–219822, NASA, Hampton, VA, 2018.

- [8] Zanetti, R., DeMars, K. J., and Bishop, R. H., “Underweighting Nonlinear Measurements,” *AIAA Journal of Guidance, Control, and Dynamics*, Vol. 33, No. 5, 2010, pp. 1670–1675. <https://doi.org/10.2514/1.50596>, URL <https://arc.aiaa.org/doi/epdf/10.2514/1.50596>.
- [9] Awad, O. F., “An Autonomous Small Satellite Navigation System for Earth, Cislunar Space, and Beyond,” Ph.D., Purdue University, United States – Indiana, 2023. URL <https://www.proquest.com/docview/2827701519/abstract/95434E3F30A942FBPQ/1>, iSBN: 9798379664848.
- [10] Awad, O., Stoeckle, M., and Oguri, K., “An Autonomous Planetary Navigation System Independent of GNSS and Ground Station Tracking,” *The Journal of the Astronautical Sciences*, Vol. 71, No. 1, 2024, p. 5. <https://doi.org/10.1007/s40295-023-00397-5>, URL <https://doi.org/10.1007/s40295-023-00397-5>.
- [11] Liao, A. R., and Oguri, K., “Shape Model-Independent Autonomous Asteroid Navigation: Analysis on Observability and Feasibility,” *Astrodynamics Specialist Conference*, American Astronomical Society, Broomfield, CO, 2024, p. 20.
- [12] Schuster, M., and Oh, S., “Three-Axis Attitude Determination from Vector Observations,” *AIAA Journal of Guidance and Control*, Vol. 4, No. 1, 1981, pp. 70–77. <https://doi.org/10.2514/3.19717>, URL <https://arc.aiaa.org/doi/epdf/10.2514/3.19717>.
- [13] Crassidis, J. L., Alonso, R., and Junkins, J. L., “Optimal Attitude and Position Determination from Line-of-Sight Measurements,” *The Journal of the Astronautical Sciences*, Vol. 48, No. 2, 2000, pp. 391–408. <https://doi.org/10.1007/BF03546286>, URL <https://doi.org/10.1007/BF03546286>.
- [14] Wertz, J., *Spacecraft Attitude Determination and Control*, Vol. 73, D. Reidel Publishing Company, Dordrecht, Netherlands, 1978.
- [15] Wahba, G., “A Least Squares Estimate of Satellite Attitude,” *SIAM Review*, Vol. 8, No. 3, 1966, pp. 384–386. <https://doi.org/10.1137/1008080>, URL <https://epubs.siam.org/doi/10.1137/1008080>, publisher: Society for Industrial and Applied Mathematics.
- [16] Davenport, P. B., “A Vector Approach to the Algebra of Rotations with Applications,” Technical Report X-546-65-437, NASA, 1965.
- [17] Keat, J. E., “Analysis of Least-Squares Attitude Determination Routine DOAOP,” Tech. Rep. CSC/TM-77/6034, Computer Sciences Corporation, 1977.
- [18] Jarrett-Izzi, E. M., “Moon-Based Non-Gaussian Multi-Object Tracking for Cislunar Space Domain Awareness,” thesis, Purdue University Graduate School, Apr. 2024. <https://doi.org/10.25394/PGS.25586988.v1>, URL https://hammer.purdue.edu/articles/thesis/Moon-Based_Non-Gaussian_Multi-Object_Tracking_for_Cislunar_Space_Domain_Awareness/25586988/1.
- [19] Jarrett-Izzi, E., Oguri, K., Carpenter, M., and Danis, J., “Investigation on Moon-based Sensor Placement for Cislunar Orbit Determination with Exclusion Zones,” *AAS Guidance, Navigation, and Control Conference*, American Astronomical Society, Breckenridge, CO, 2024, p. 20.

- [20] Spreen, E. M. Z., “Trajectory Design and Targeting for Applications to the Exploration Program in Cislunar Space,” Ph.D., Purdue University, United States – Indiana, 2021. URL <https://www.proquest.com/docview/2838330965/abstract/88F8315D820B498FPQ/1>, iISBN: 9798379829155.
- [21] Christian, J., “Relative Navigation Using Only Intersatellite Range Measurements,” *AIAA Journal of Spacecraft and Rockets*, Vol. 54, No. 1, 2017, pp. 13–28. <https://doi.org/https://doi.org/10.2514/1.A33608>, URL <https://arc.aiaa.org/doi/epdf/10.2514/1.A33608>.
- [22] Hill, K., and Born, G., “Autonomous Interplanetary Orbit Determination Using Satellite-to-Satellite Tracking,” *Journal of Guidance, Control, and Dynamics*, Vol. 30, No. 3, 2007, pp. 679–686. <https://doi.org/10.2514/1.24574>, URL <https://arc.aiaa.org/doi/epdf/10.2514/1.24574>.
- [23] Hostetler, J., and Cowardin, H., “Experimentally-Derived Phase Function Approximations in Support of the Orbital Debris Program Office,” *International Orbital Debris Conference*, Sugar Land, TX, 2019.
- [24] Cunningham, F., “Earth Reflected Solar Radiation Input to Spherical Satellites,” *ARS Journal*, Vol. 32, No. 7, 1962, pp. 1033–1036. <https://doi.org/10.2514/8.6199>, URL <https://arc.aiaa.org/doi/epdf/10.2514/8.6199>.
- [25] Frueh, C., *Space Traffic Management*, 5th ed., Purdue University, 2022.
- [26] “PYTHON 25K/16K Global Shutter CMOS Image Sensors, NOIP1SN025KA/D,” , 2022.
- [27] Montenbruck, O., and Gill, E., *Satellite Orbits*, 1st ed., Springer Berlin, Heidelberg, 2000.
- [28] Euler, L., “Formulae Generales pro Translatione Quacunque Corporum Rigidorum,” *Novi Commentarii academiae scientiarum Petropolitanae*, Vol. 20, 1776, pp. 189–207.
- [29] Meyer Jr., C. D., “Generalized Inversion of Modified Matrices,” *SIAM Journal of Applied Mathematics*, Vol. 24, No. 3, 1973, pp. 315–323. <https://doi.org/10.1137/0124033>, URL <https://epubs.siam.org/doi/epdf/10.1137/0124033>.
- [30] KNOCKE, P., RIES, J., and TAPLEY, B., “Earth radiation pressure effects on satellites,” *Astrodynamics Conference*, American Institute of Aeronautics and Astronautics, 1988, pp. 577–587. <https://doi.org/10.2514/6.1988-4292>, URL <https://arc.aiaa.org/doi/abs/10.2514/6.1988-4292>, _eprint: <https://arc.aiaa.org/doi/pdf/10.2514/6.1988-4292>.
- [31] Taylor, J. H., “The Cramer-Rao estimation error lower bound computation for deterministic nonlinear systems,” *Conference on Decision and Control including the 17th Symposium on Adaptive Processes*, 1978, pp. 1178–1181. <https://doi.org/10.1109/CDC.1978.268121>, URL <https://ieeexplore.ieee.org/document/4046308/?arnumber=4046308>.